

DNA 5055F

# MHDEMP CODE SIMULATION OF STARFISH

LEVEL 11

12

Steven Chavin  
William F. Crevier  
Ralph W. Kilb  
Conrad L. Longmire  
Mission Research Corporation  
P.O. Drawer 719  
Santa Barbara, California 93102

DTIC  
ELECTRONIC  
S OCT 26 1981  
E

1 August 1979

Final Report for Period 7 March 1978—1 August 1979

CONTRACT No. DNA 001-78-C-0193

APPROVED FOR PUBLIC RELEASE;  
DISTRIBUTION UNLIMITED.

THIS WORK SPONSORED BY THE DEFENSE NUCLEAR AGENCY  
UNDER RDT&E RMSS CODE B323078464 R99QAXEA09183 H2590D.

Prepared for  
Director  
DEFENSE NUCLEAR AGENCY  
Washington, D. C. 20305

81 10 26 069

AD A106089

DTIC FILE COPY

Destroy this report when it is no longer needed. Do not return to sender.

PLEASE NOTIFY THE DEFENSE NUCLEAR AGENCY,  
ATTN: STT1, WASHINGTON, D.C. 20305, IF  
YOUR ADDRESS IS INCORRECT, IF YOU WISH TO  
BE DELETED FROM THE DISTRIBUTION LIST, OR  
IF THE ADDRESSEE IS NO LONGER EMPLOYED BY  
YOUR ORGANIZATION.



UNCLASSIFIED

SECURITY CLASSIFICATION OF THIS PAGE (When Data Entered)

19 REPORT DOCUMENTATION PAGE		READ INSTRUCTIONS BEFORE COMPLETING FORM	
1. REPORT NUMBER DNA 5055F	2. GOVT ACCESSION NO. AD-A106084	3. RECIPIENT'S CATALOG NUMBER 084	
4. TITLE (and Subtitle) MHDEMP CODE SIMULATION OF STARFISH		5. TYPE OF REPORT & PERIOD COVERED Final Report for Period 7 Mar 78-1 Aug 79	
6. AUTHOR(s) Steven Chavin William F. Crevier		7. PERFORMING ORG. REPORT NUMBER MRC-R-516	
8. AUTHOR(s) Ralph W. Kilb Conrad L. Longmire		9. CONTRACT OR GRANT NUMBER(s) DNA 001-78-C-0193	
9. PERFORMING ORGANIZATION NAME AND ADDRESS Mission Research Corporation P. O. Drawer 719 Santa Barbara, California 93102		10. PROGRAM ELEMENT PROJECT TASK AREA & WORK UNIT NUMBERS Subtask R99QAXEA091-83	
11. CONTROLLING OFFICE NAME AND ADDRESS Director Defense Nuclear Agency Washington, D.C. 20305		12. REPORT DATE 1 August 1979	
14. MONITORING AGENCY NAME & ADDRESS (if different from Controlling Office) 12-17		13. NUMBER OF PAGES 56	
		15. SECURITY CLASS (of this report) UNCLASSIFIED	
		15a. DECLASSIFICATION DOWNGRADING SCHEDULE N/A	
16. DISTRIBUTION STATEMENT (of this Report)  Approved for public release; distribution unlimited.			
17. DISTRIBUTION STATEMENT (of the abstract entered in Block 20, if different from Report)			
18. SUPPLEMENTARY NOTES This work sponsored by the Defense Nuclear Agency under RDT&E RMSS Code B323078464 R99QAXEA09183 H2590D.			
19. KEY WORDS (Continue on reverse side if necessary and identify by block number) Magnetohydrodynamic EMP      Geomagnetic Field Variations Electromagnetic Pulse (EMP)      Starfish Nuclear Effects High Altitude EMP			
20. ABSTRACT (Continue on reverse side if necessary and identify by block number) The magnetic field variations on the ground after Starfish are calculated by the MHDEMP code using input parameters produced by the MICE code. The results agree well with the experimental data at Johnston Island. These magnetic field variations extend over large distances and may cause large potential fluctuations in long-line ground systems.			

DD FORM 1 JAN 73 1473

EDITION OF 1 NOV 65 IS OBSOLETE

UNCLASSIFIED

SECURITY CLASSIFICATION OF THIS PAGE (When Data Entered)

406541

41

## PREFACE

We thank Fredric E. Fajen for providing us with MICE code output and many useful discussions concerning the structure of the MICE code.

Accession For		
NTIS GRA&I	<input checked="checked" type="checkbox"/>	
DTIC TAB	<input type="checkbox"/>	
Unannounced	<input type="checkbox"/>	
Justification		
By		
Distribution/		
Availability Codes		
Avail and/or		
Dist	Special	
A		

## TABLE OF CONTENTS

PREFACE	1
LIST OF ILLUSTRATIONS	3
SECTION	
1 INTRODUCTION	5
2 THE MHDMP CODE	8
3 STARFISH SIMULATION	14
4 ADDITIONAL CALCULATIONS	31
5 CONCLUSIONS AND POSSIBLE FUTURE IMPROVEMENTS	37
REFERENCES	39
APPENDIX	41

## LIST OF ILLUSTRATIONS

<u>Figure</u>	<u>Page</u>
1. Sketch of $\Delta \vec{B}$ and surface current rings in ground.	16
2. $ \Delta \vec{B} $ on ground. Times: 30.0, 36.34, 40.0 seconds.	17
3. $ \Delta \vec{B} $ on ground. Times: 50.0, 60.0, 69.2 seconds.	18
4. $ \Delta \vec{B} $ on ground. Times: 90.0, 100.0, 110.0 seconds.	19
5. $\Delta  \vec{B} $ on ground. Times: 24.6, 30.0, 40.0 seconds.	21
6. $\Delta  \vec{B} $ on ground. Times: 50.0, 60.0, 69.2 seconds.	22
7. $\Delta  \vec{B} $ on ground. Times: 90.0, 100.0, 110.0 seconds.	23
8. $\vec{J}_y$ in symmetry plane. Times: 24.6, 40.0, 60.0 seconds.	24
9. $\vec{J}_y$ in symmetry plane. Times: 69.2, 90.0, 100.0 seconds.	25
10. Time plot of $\Delta  \vec{B} $ at $x = -184$ km.	27
11. Time plot of $\Delta  \vec{B} $ at $x = 23.4$ km.	28
12. Time plot of $\Delta  \vec{B} $ at $x = 179.2$ km.	29
13. $\vec{J}_y$ in symmetry plane for standard MICE $N_e$ and standard beta patch. Times: 40.0, 69.2, 110.0 seconds.	33
14. $\Delta  \vec{B} $ on ground. Standard MICE $N_e$ and standard beta patch. Times: 50.0, 69.2, 110.0 seconds.	34
15. $\Delta  \vec{B} $ on ground for MICE $N_e/3$ . Times: 50.0, 69.2, 110.0 seconds.	36

## SECTION 1

### INTRODUCTION

A high altitude nuclear explosion like the 1962 burst Starfish (400 km altitude) generates large currents in the ionosphere. These currents, like the current in a normal wire, produce magnetic fields at points far away from the region where the actual currents flow. When these magnetic fields reach the surface of the earth they set up electric fields and currents in the soil (or ocean). A long conducting wire in this region may experience a large voltage drop across widely separated ground connections, which can interrupt the line's function.

The source of the ionospheric currents is the magneto-hydrodynamic (MHD) motion of the ionized air surrounding the burst point. The term MHD/EMP has been coined to distinguish this effect from the EMP generated by other mechanisms. To calculate the MHD/EMP signal one first needs to calculate the current patterns generated by a nuclear explosion in the ionosphere. One also needs to characterize the soil where the long lines are located to relate the incident magnetic field to an induced electric field.

For the past few years the DNA MHD/EMP program has been directed at attacking these two problems. MRC has been primarily involved with the calculation of the current patterns. Our efforts have involved both trying to develop simple models for the ionosphere currents<sup>1</sup> and actually trying to compute the currents for nuclear events such as Starfish<sup>2,3</sup>. The modeling only met with limited success because of the complex nature of the current patterns. However, it did lead us to conclude that there were several distinct mechanisms responsible for the signals measured after the

high altitude events during the 1962 test series (see the Appendix). In particular, Longmire<sup>4</sup> concluded that the 700 gamma ( $7 \times 10^{-3}$  gauss) signal observed about 70 seconds after the Starfish event was due to the upward motion (heave) of the atmosphere below the burst point. This air, which is initially between 90 and 150 km altitude, is heated by x-rays and by energetic ions which travel down the magnetic field lines from the burst point. These regions of heated air are called the x-ray patch and the kinetic energy (or debris) patch.

The motion of the air after the burst is computed using the 3-D MHD code MICE<sup>5</sup>. MICE is designed primarily as a radar and communication effects code so the emphasis is on correctly computing electron densities. Electric and magnetic fields are computed since they influence the motion of the plasma, but with approximations which produce somewhat inaccurate results over much of the grid. Previous attempts to use MICE to compute MHD/EMP effects were generally unsuccessful<sup>2,3</sup>. For the present effort we spent some time trying to change MICE to do a better job at computing the magnetic fields but finally decided on a new approach.

To solve for the MHD/EMP at the surface of the earth we use the neutral wind velocities and the ion and neutral densities computed from MICE (quantities it was designed to compute accurately) as input to a SIMPLE 3-D Maxwell equation solver. The Maxwell solver (MHDEMP) is optimized to solve for the electric and magnetic fields that result from the atmospheric motion computed by MICE.

Using this combination of MICE and the MHDEMP code we were able, for the first time, to compute accurate magnetic fields at the surface of the earth for the Starfish event. We obtained excellent agreement with the measured signal at Johnston Island (see Figure 12, pg 27). It is dangerous to conclude from one measurement that our analysis is correct at all other locations but before the technique was developed there was



not even agreement at the one point. We have demonstrated that we understand the mechanism responsible for the large, late time, magnetic pulse seen after Starfish and that we can compute the observed signal from first principles. As we have time to study the computer output and increase our understanding of the phenomena we will be able to develop more confidence in the results at other points and for other bursts.

In Section 2 we briefly explain the operation of the MHD/EMP code. Since this section will only be of interest to someone familiar with the high altitude MHD equations we have assumed a working knowledge of the terms and equations generally used in that field. (See Chapter 12 of Reference 6 for example.)

Three separate MHD/EMP simulations were made for this report. The first simulation used the standard MICE plasma parameters as input. This gave the best results and is presented in Section 3. The basic MICE calculation does not include the ionization produced by  $\beta$ -particles which are emitted by the bomb debris and spiral down the magnetic field lines to an altitude of 60 to 80 km making what is called a beta patch. It was felt that this ionization should be important to the MHD/EMP signal so an additional run was made which included the beta patch. Also there was some thought that the MICE electron densities might be as much as a factor of three too high so a third simulation was run with the MICE conductivities artificially set a factor of three smaller. A beta patch was also included for this third simulation. The results of these two additional simulations are included in Section 4.

A summary of the results is presented in Section 5 along with recommendations for future work. We have also included in the Appendix a brief time history of events following a high altitude nuclear burst relevant to the MHD/EMP problem. A reader not familiar with all the phenomena involved might benefit from reading the Appendix before reading the following sections.

## SECTION 2

### THE MHDEMP CODE

Although it does not appear feasible to use the MICE currents directly to compute  $\vec{B}$  on the ground, we believe the other plasma parameters from MICE are very reliable. The new MHDEMP code computes  $\vec{B}$  on the ground using the neutral heave and conductivities from MICE. The MHDEMP code is a straightforward 3-D code, which can be rapidly iterated many times. The grid extends to the ground so the  $\vec{B}$ -field there can be computed directly. Our immediate objective was to use the co-e to calculate the large negative signal measured on the ground 70 seconds after the Starfish event. It appears the code is capable of computing the earlier positive signal, as well.

The MHDEMP code's basic assumption is that the electromagnetic forces balance the neutral drag force. This is the same basic assumption used for the MICE code and other MHD codes, except that usually other forces are included in addition to the neutral drag force. The MICE code includes inertia, gravity, and the pressure gradient force. These forces should not be important for our times of interest. The resultant equation for the current is<sup>6</sup>

$$\vec{J} = \sigma_{\parallel} \vec{E}_{\parallel} + \sigma_p \left( \vec{E}_{\perp} + \frac{\vec{V}_n \times \vec{B}}{c} \right) - \sigma_H \left( \vec{E} \times \hat{b} - \frac{B}{c} \vec{V}_{n\perp} \right) \quad (1)$$

where we have introduced the three well known conductivities:

$$\text{Parallel } \sigma_{\parallel} = \frac{eN}{B} \left[ \frac{1 + \eta_{eo}/\eta_{io}}{\eta_{eo} + \eta_{ei} (1 + \eta_{eo}/\eta_{io})} \right] \quad (2)$$

$$\text{Pedersen } \sigma_P = \frac{eN}{B} \left[ \frac{(\eta_{io} + \eta_{eo}) [1 + \eta_{io}\eta_{eo} + \eta_{ei}(\eta_{io} + \eta_{eo})]}{(1 + \eta_{io}^2)(1 + \eta_{eo}^2) + \eta_{ei}(\eta_{io} + \eta_{eo}) [2 + 2\eta_{io}\eta_{eo} + \eta_{ei}(\eta_{io} + \eta_{eo})]} \right] \quad (3)$$

$$\text{Hall } \sigma_H = \frac{eN}{B} \left[ \frac{\eta_{io}^2 - \eta_{eo}^2}{(1 + \eta_{io}^2)(1 + \eta_{eo}^2) + \eta_{ei}(\eta_{io} + \eta_{eo}) [2 + 2\eta_{io}\eta_{eo} + \eta_{ei}(\eta_{io} + \eta_{eo})]} \right] \quad (4)$$

The  $\eta$ 's are dimensionless ratios of gyro frequency to momentum transfer collision frequency:  $\eta_{io} \equiv \nu_{io}/\Omega_i$ ,  $\eta_{eo} \equiv \nu_{eo}/\Omega_e$  and  $\eta_{ei} \equiv \nu_{ei}/\Omega_e$ .

One can invert Equation 1 to obtain  $\vec{E}$ .

$$\begin{aligned} \vec{E}_{||} &= \frac{1}{\sigma_{||}} \vec{J}_{||} \\ &= \frac{1}{4\pi\sigma_{||}} \left( (\nabla \times \vec{B})_{||} - \frac{\epsilon}{c} \frac{\partial \vec{E}_{||}}{\partial t} \right) \end{aligned} \quad (5)$$

$$\begin{aligned} \vec{E}_{\perp} &= \frac{\sigma_P}{(\sigma_P^2 + \sigma_H^2)} \vec{J}_{\perp} - \frac{\vec{V}_n \times \vec{B}}{c} - \frac{\sigma_H}{(\sigma_P^2 + \sigma_H^2)} \vec{J}_{\perp} \times \hat{b} \\ &\approx \frac{\sigma_P}{4\pi(\sigma_P^2 + \sigma_H^2)} \left( (\nabla \times \vec{B})_{\perp} - \frac{\epsilon}{c} \frac{\partial \vec{E}_{\perp}}{\partial t} \right) - \frac{\vec{V}_n \times \vec{B}}{c} \end{aligned} \quad (6)$$

The second lines of Equations 5 and 6 were written using one of Maxwell's Equations,  $\vec{J} = \frac{1}{4\pi} (\nabla \times \vec{B} - \frac{\epsilon}{c} \frac{\partial \vec{E}}{\partial t})$ . The second line of Equation 6 ignores the symmetry breaking Hall term, which reflects the present state of the MHDMP code. This term is believed to be an insignificant factor for most of the grid, but may be important enough from 80 km to 130 km altitude to warrant its inclusion into the code. Its omission allows the use of a symmetry plane and better resolution in the MHDMP code.

This paper uses modified Gaussian cgs units. The current density and magnetic fields are in emu, abamps  $\text{cm}^{-2}$  and Gauss, electric fields in esu, statvolts  $\text{cm}^{-1}$ . The dimensions of conductivity are  $\text{cm}^{-1}$  and the dielectric constant is dimensionless.

The code uses Equations 5 and 6 to find  $\vec{E}$  from  $\vec{B}$  and  $\vec{V}_n$  and then advances  $\vec{B}$  in time via

$$\frac{\partial \vec{B}}{\partial t} = -c \nabla \times \vec{E} \quad (7)$$

To speed execution time the MHDEMP code is very straightforward. For instance, the parallel-to- $\vec{B}$  direction for the conductivities is taken to be the ambient  $\vec{B}$  direction. It would take a large computational effort to compute the conductivity tensor with the true parallel-to- $\vec{B}$  direction, which normally is close to the ambient direction. The conductivities and  $(\vec{V}_n \times \vec{B}/c)$  terms are updated only at MICE dump times, which are spaced at 5 to 15 second intervals. These simplifications may be eliminated in the future, if more accuracy is desired.

The MHDEMP code will be unstable if the signal speed is too fast compared to the time step. The fastest signals occur in the lower atmosphere from the ground up to the altitude where significant electron density occurs, which is either the beta patch ( $\sim 60$  km) or the E-region ( $\sim 100$  km). The conductivity of the lower atmosphere is insignificant and the signal speed reduces to the speed of light in a dielectric,  $c/\sqrt{\epsilon}$ . The dielectric constant for the entire computational grid is artificially increased, so that

$$\epsilon > \frac{c(\Delta t)^2}{\Delta S_o(.8)} \quad (8)$$

where  $\Delta S_o$  is the smallest cell dimension anywhere in the MHDEMP grid and  $\Delta t$  is the time step. Typical operating parameters are  $\Delta S_o = 8$  km,

$\Delta t = 0.02$  seconds and  $\epsilon = 9 \times 10^5$ . The early development versions of the MHDMP code omitted the displacement current ( $-\frac{\epsilon}{c} \frac{\partial \vec{E}}{\partial t}$  in Equation 6 and 7) and obtained stability by introducing an artificial conductivity. The displacement current is normally omitted from MHD codes. Without the displacement current the signal speed is the 3-D magnetic diffusion speed and the stability requirement is

$$\sigma_{||} \quad \text{and} \quad \left( \frac{\sigma_p^2 + \sigma_H^2}{\sigma_p} \right) \geq \frac{c \Delta t}{(1/6) 4\pi (\Delta S)^2} \quad (9)$$

The code checked the input values of  $\sigma_{||}$  and  $\left( \frac{\sigma_p^2 + \sigma_H^2}{\sigma_p} \right)$  in every cell and increased them to the minimum stable value, if necessary. The  $\Delta S$  is the smallest of the three cell dimensions  $\Delta x$ ,  $\Delta y$  or  $\Delta z$ . This method is analogous to the Boris mass modifications<sup>7</sup> of the MICE code (where the signal speed is the Alfvén speed) and also results in artificially high currents in regions where the conductivities should be low.

The artificial conductivities proved to be a significant liability. Not only were the currents artificially increased in peripheral regions of the grid, but a sizeable amount of current was able to flow through the lower atmosphere into the bottom boundary of the grid. This introduced spurious magnetic fields on the ground comparable in magnitude to the expected fields. Decreasing the time step and adding a special resistive layer helped slightly, while increasing computer costs a great deal. For this reason we introduced the displacement current. The conduction current flowing through the lower atmosphere is now a factor of  $10^4$  less than in the early versions of the code.

The location of the top boundary is chosen so that no signal generated above the top boundary has time to diffuse to the ground by the end of the simulation. Presently, the perfectly conducting ground and the symmetry plane use the boundary condition

$$\hat{n} \times \vec{J} = 0 . \quad (10)$$

The top and other side boundaries obey

$$\hat{n} \cdot \vec{J} = 0 \quad (11)$$

to keep current from leaving the grid.

The beta patch is ignored by MICE, since it lies below the bottom of the MICE grid. The MHDMP code uses a beta patch model previously used by Crevier combined with some features of a model by Longmire<sup>8</sup>. The power into betas is

$$P_{\beta} = \frac{(.15)(.05)\omega_f}{(1+t)1.15} \text{ ergs/sec} \quad (12)$$

where  $\omega_f$  is the fission yield, the .05 represents the 5% of fission yield into betas and the 0.15 is a normalizing factor. The rate of ion-pair production in the beta patch is

$$\dot{n} = \frac{f_{\beta} P_{\beta} 0.5 \times \rho_n \times \sqrt{2} \times 1.6}{(1.7 \times 35 \times 1.6 \times 10^{-12})} \text{ cm}^{-3} \text{ sec}^{-1} \quad (13)$$

The assumptions that lead to Equation 13 are as follows. The beta energy is taken to be 1.7 MeV. The energy loss rate is  $(1.6 \text{ MeV cm}^2/\text{gram})\rho_n$ . An ion-electron pair is formed for every 35 eV deposited by the betas. One half of the betas go up and one half go down. The  $\sqrt{2}$  comes from the assumption that the betas spiral around the field lines with a pitch angle of 45°. The large pitch angle is due to the magnetic mirror effect, since the betas travel from a region where the fields are weak to the ambient field.

The relative number of betas on each field line is determined by  $f_{\beta}(\text{cm}^{-2})$ . Longmire's model<sup>8</sup> for  $f_{\beta}$  when applied to Starfish yields

$$f_{\beta} = \frac{1}{4\pi S_0^2} \sqrt{1+1.64(S/S_0)} e^{-S/S_0} \quad (14)$$

where  $S$  is the distance from the burst point field line to the field line in question and  $S_0$  is 60 km.

The equilibrium electron density is determined from  $\dot{n}$  by lumping the deionization chemistry into a single recombination rate

$$n = \sqrt{\frac{\dot{n}}{\alpha}} ; \quad \alpha = 3 \times 10^{-7} \text{ cm}^3/\text{sec} \quad (15)$$

The peak ionization occurs at 60 km where the bulk of the beta energy is deposited. Ionization due to betas above 100 km or below 60 km is ignored. To compute conductivities below the bottom of the MICE grid (77 km), ambient electron temperatures and neutral densities are assumed. The grid spacing for the Starfish run described in Section 3 was 8 km in the beta patch region, which is too coarse to resolve the beta patch at the ionization peak. A finer grid spacing would be better.

### SECTION 3

#### STARFISH SIMULATION

This section describes a Starfish simulation using the MHDEMP code. Starfish was chosen, since among the Fishbowl events, it had the largest signal and represents the greatest threat to long-line systems. In addition, a recent MICE Starfish calculation had just been completed out to 105 seconds. F. E. Fajen kindly made these results available to us. While we were in the midst of performing the MHDEMP simulations, a new MICE Starfish run was announced for later this year. It is anticipated that the new Starfish results could have a factor of 3 lower electron densities in the debris patch. Our first MHDEMP simulation used the existing MICE plasma parameters and the beta patch model explained in Section 2. The second simulation had the same beta patch and MICE parameters except the MICE electron densities were decreased by a factor of 3. This was done to check the sensitivity of the results to  $N_e$  in anticipation of the future MICE Starfish run. The third simulation was the same as the first, except the beta patch was excluded. The third simulation gives the best fit to the J.I. data and will be described in depth. The results of the first two simulations will be discussed in Section 4. All figures in this section will come from the third simulation, i.e., without the beta patch.

The simulations starts at 20 seconds with  $\vec{B}$  ambient everywhere. The MHDEMP grid is the same as the MICE grid (+ x is north; + y is west, + z is up), except the bottom of the MHDEMP is at  $z = 0$  rather than  $z = 77$  km and the top is at  $z = 400$  km rather than  $z = 1024$  km. Signals generated above 400 km are not expected to propagate to the ground by the end of the simulation at 110 seconds. The origin of the coordinate system ( $x=0$ ,  $y=0$ ,  $z=0$ ) is located on the ground directly beneath the burst point. Johnston Island is at ( $x = 30$  km,  $y = 0$ ,  $z = 0$ ). The time step was 0.02 seconds and  $\epsilon = 9 \times 10^5$  was needed for stability.



Page 44 shows Longmire's prediction of the current patterns in the ground and in the debris patch, which agrees for the most part with the result of the MHDTEMP code. The rising neutrals operate as a homopolar generator. From Equation 1 one would expect a westward current in response to the  $\vec{V}_n \times \vec{B}/c$  term. This current must find an eastward return path. The current will diminish or stop depending upon the magnitude of an opposing  $\vec{E}_\perp$ , if such an  $\vec{E}_\perp$  is able to be established. The current is expected to flow along field lines in regions where  $\sigma_\parallel \gg ((\sigma_p^2 + \sigma_H^2)/\sigma_p)$  and is able to cross field lines easily where  $(\sigma_p^2 + \sigma_H^2)/\sigma_p$  is large. Therefore, the illustration on page 44 shows the current flowing predominately down field lines and returning to the east at lower altitudes where  $(\sigma_p^2 + \sigma_H^2)/\sigma_p$  is large. The illustration shows another loop to the south which is above the burst point and originally was meant to represent the southern conjugate point. Our simulation had a similar current pattern in the debris patch and on the ground with some exceptions. The southern current loop was not above the generator region, but was below the generator region. Also there exists another load region not predicted in the illustration on page 44.

Figure 1 shows a sketch of the perturbed field  $\vec{\Delta B}$  on the ground at 69.2 seconds. Also shown is the direction of the surface currents induced in the ground to keep the perturbed magnetic field from penetrating the perfectly conducting ground. The surface current is perpendicular to  $\vec{\Delta B}$  and flows in two opposing rings. For an earth with a large finite conductivity the values of the surface current would be computed via Stokes's Law from  $|\vec{\Delta B}|$ , if the skin depth is known. Letting  $\vec{\Delta B} = 0$  one skin depth inside the earth and if  $\vec{\Delta B}$  is parallel to the earth's surface,

$$\langle J \rangle = \frac{|\vec{\Delta B}|}{4\pi h} \quad (16)$$

where  $\langle J \rangle$  is the current density averaged over a skin depth  $h$  and  $|\vec{\Delta B}|$  is evaluated at the earth's surface. Figures 2 to 4 shows  $|\vec{\Delta B}|$  on the ground at various times. We expect the difference between a

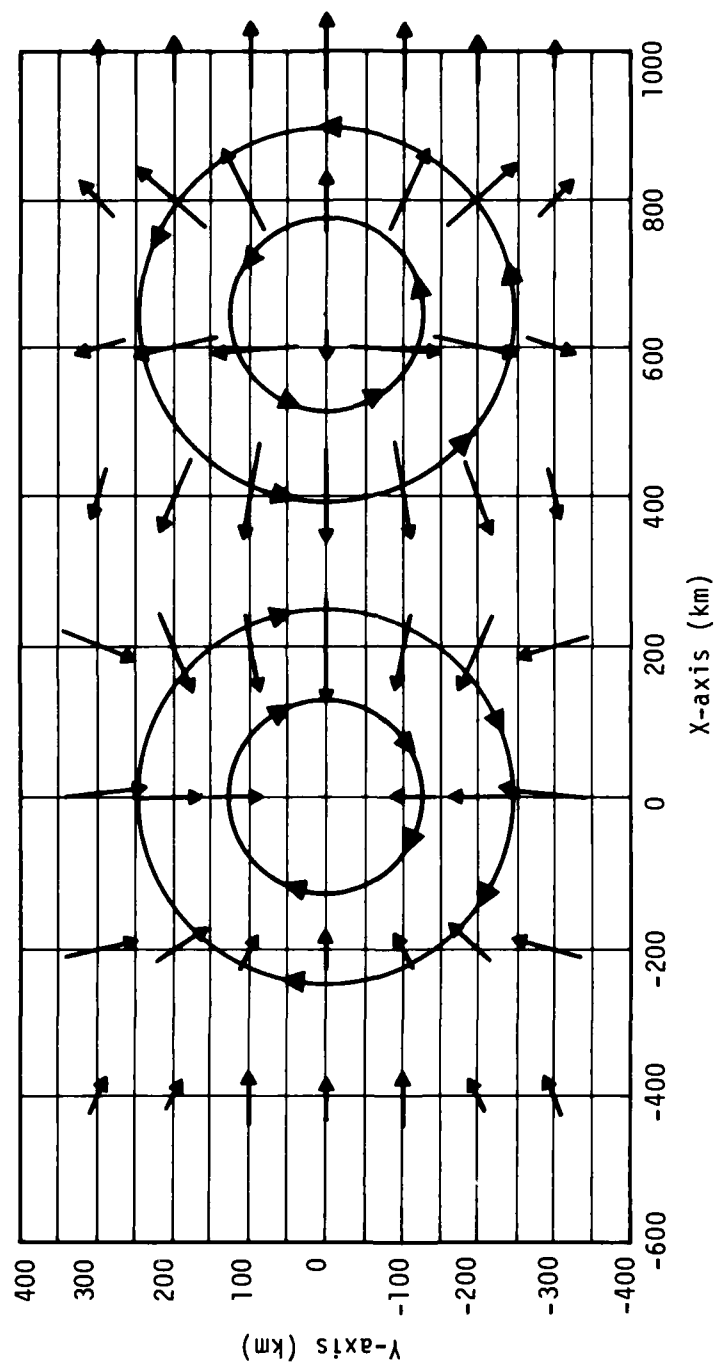


Figure 1. Sketch of  $\vec{\Delta B}$  vectors and surface current rings on the ground at 69.2 seconds. The entire grid is shown for clarity. The  $y=0$  axis is a symmetry axis.

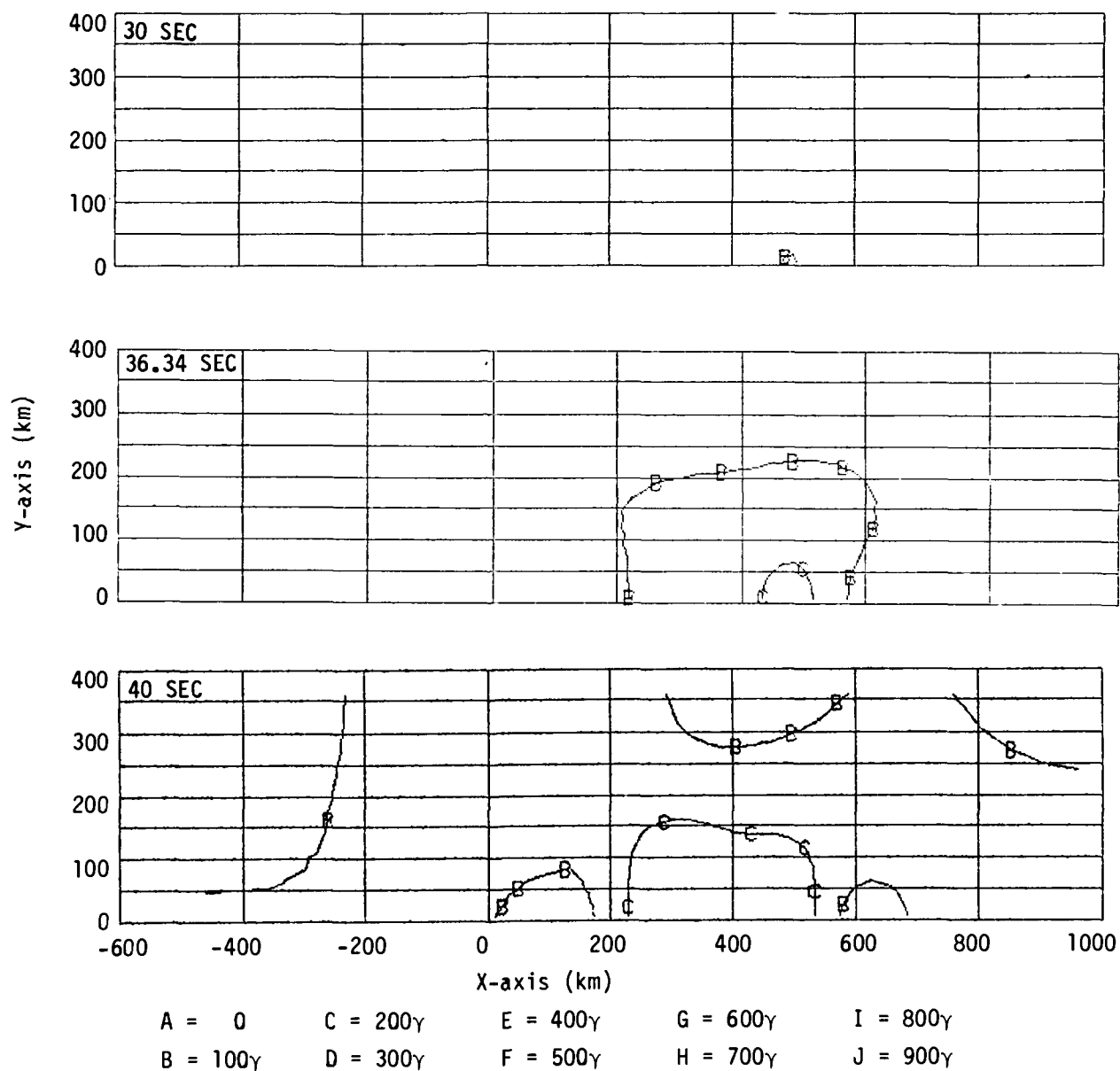


Figure 2.  $|\vec{\Delta B}|$  on the ground at 30.0, 36.34, 40.0 seconds. MICE  $N_e$  without beta patch.

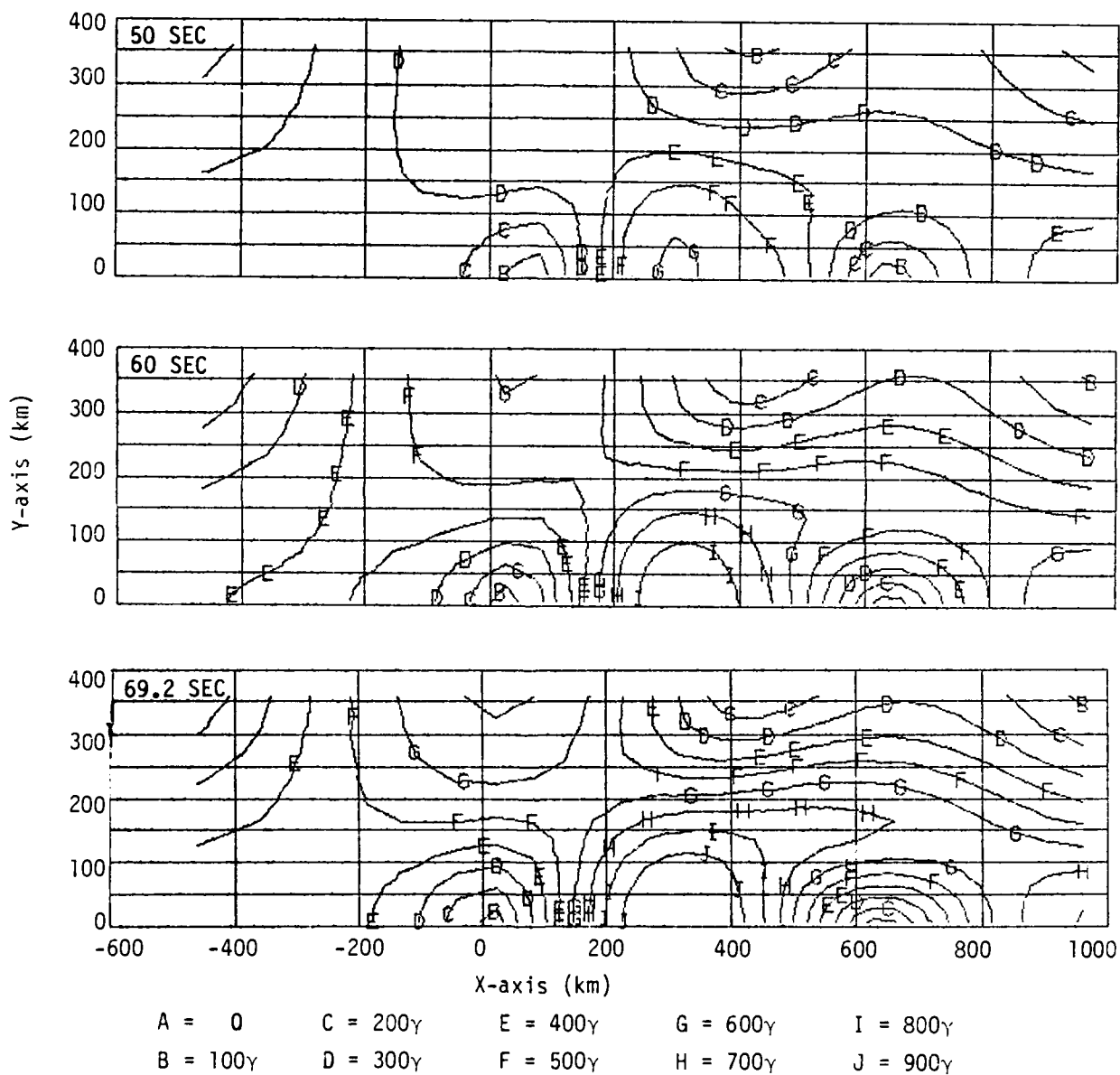


Figure 3.  $|\Delta \vec{B}|$  on the ground at 50.0, 60.0, 69.2 seconds. MICE  $N_e$  without beta patch.

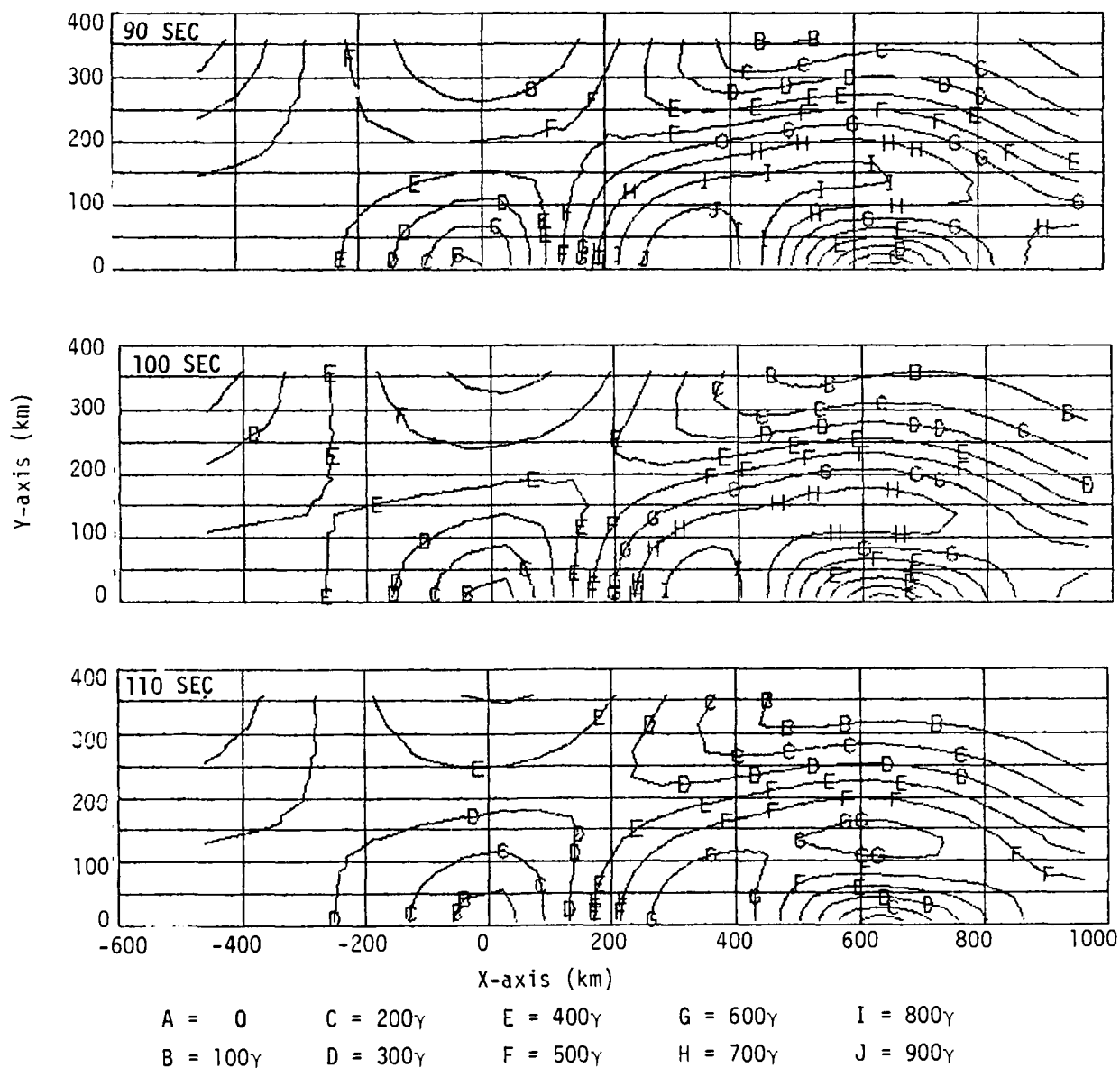


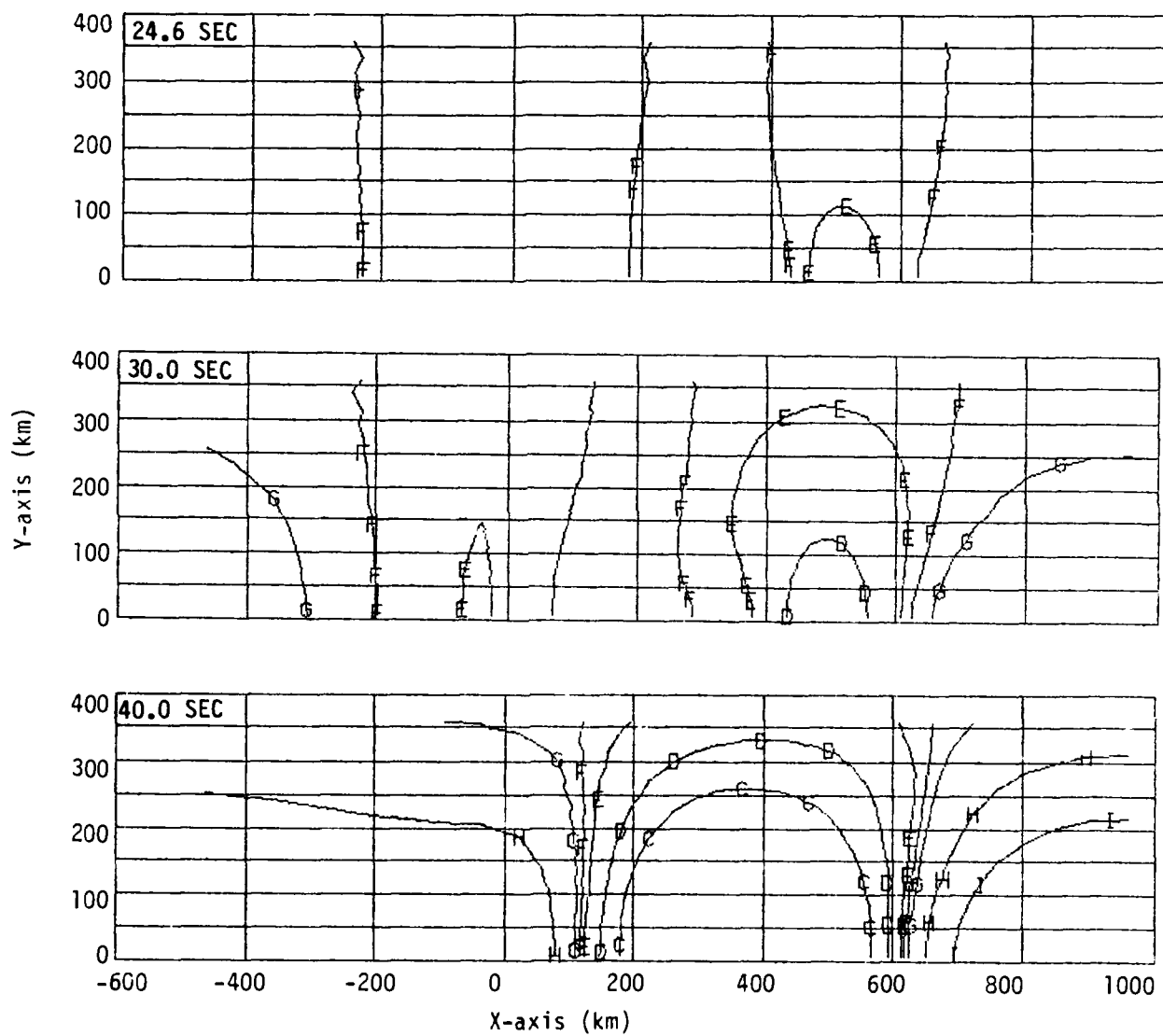
Figure 4.  $|\Delta \vec{B}|$  on the ground at 90.0, 100.0, 110.0 seconds. MICE  $N_e$  without beta patch.

perfectly conducting boundary and a realistic conducting ocean should not affect these values appreciably.

The magnetometer at J.I. measured the change in the magnitude of the total magnetic field  $\vec{B}$ , ambient plus perturbed. Figures 5 to 7 show the change relative to ambient of the total field on the ground  $\Delta|\vec{B}| = |\vec{B}_A + \Delta\vec{B}| - |\vec{B}_A|$ . The early times are influenced by the fact that the simulation started at 20 seconds with ambient  $\vec{B}_A$ . The pattern of the field on the ground sketched in Figure 1 sets in by 40 seconds and remains unchanged for the rest of the run. In the central region where  $\Delta\vec{B}$  points generally south,  $|\vec{B}|$  is decreased. On the south ( $x = -600$  km to  $x = 0$ ) and the north ( $x = 600$  km to  $x = 1000$  km) ends of the grid,  $\Delta\vec{B}$  points generally north and  $|\vec{B}|$  is increased.

Between the regions of positive  $\Delta|\vec{B}|$  and negative  $\Delta|\vec{B}|$  are two node lines. Magnetometers sitting on a node would indicate no change in the magnitude of the magnetic fields. J.I. is close to the southern node line.

From the prediction on page 44 one would expect to see a two ring current pattern in the debris patch. The actual 3-D geometry is more complicated than the simple discrete circuit pictured on page 44. In our simulation there is no sharp distinction between the northern and southern load regions. Figures 8 and 9 show  $\vec{J}_y$  in the symmetry plane. There is a load region (eastward current) immediately below the main generator region due to slower upward winds there. This load was not predicted on page 44. There is another load region in the E-region at 100 km altitude. Both the southern and northern loads are at this altitude. Some of the current flows directly east into the symmetry plane after reaching the E-region. This major return path centered around  $x = 400$  km corresponds directly to the northern return path on page 44. Since this region is



A = -1000γ	C = - 100γ	E = - 10γ	G = 10γ	I = 100γ
B = - 500γ	D = - 50γ	F = 0	H = 50γ	J = 500γ

Figure 5.  $|\Delta \vec{B}|$  on the ground at 24.6, 30.0, 40.0 second. MICE  $N_e$  without beta patch.

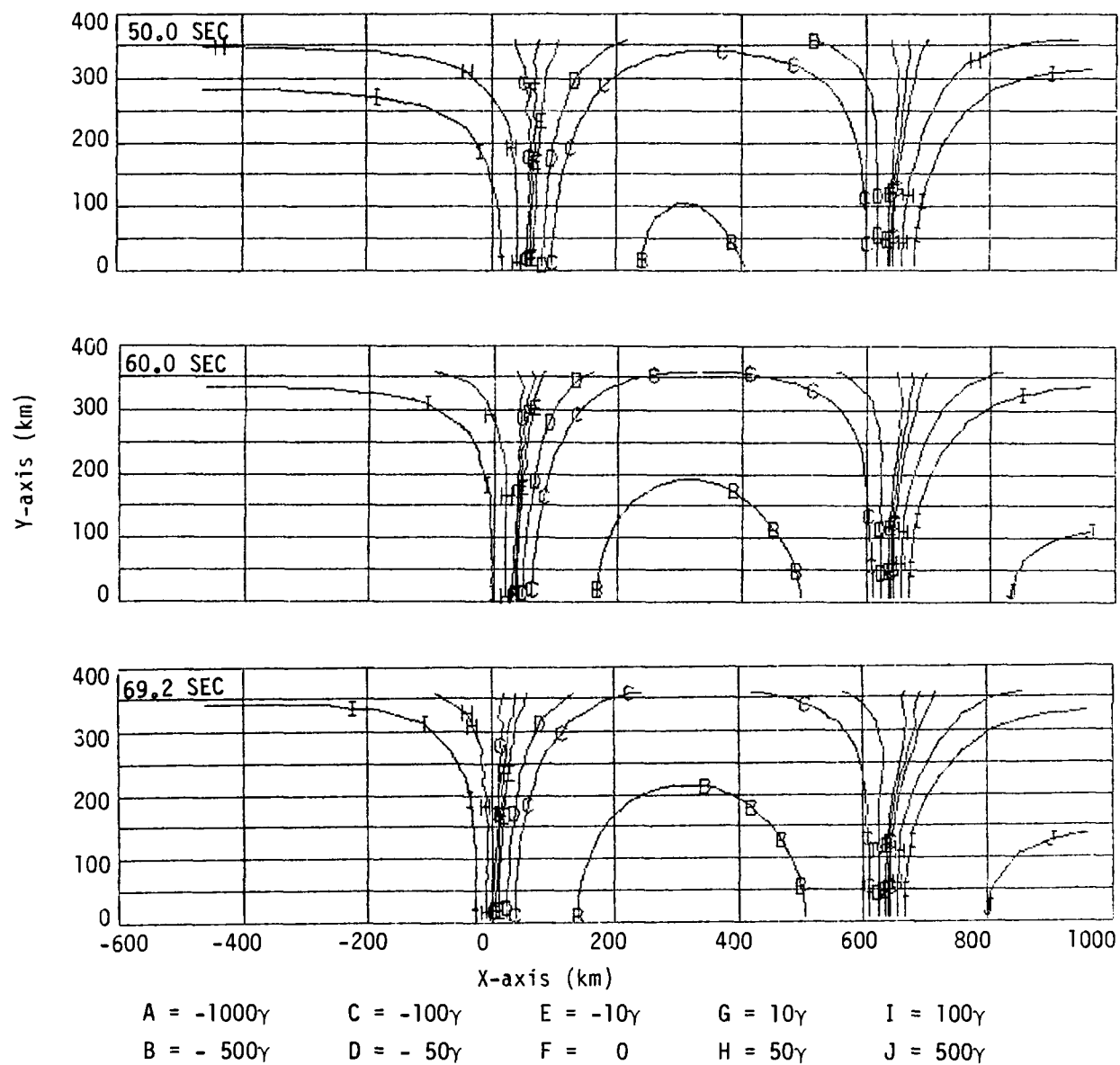


Figure 6.  $\Delta|\vec{B}|$  on the ground at 50.0, 60.0, 69.2 seconds. MICE  $N_e$  without beta patch.



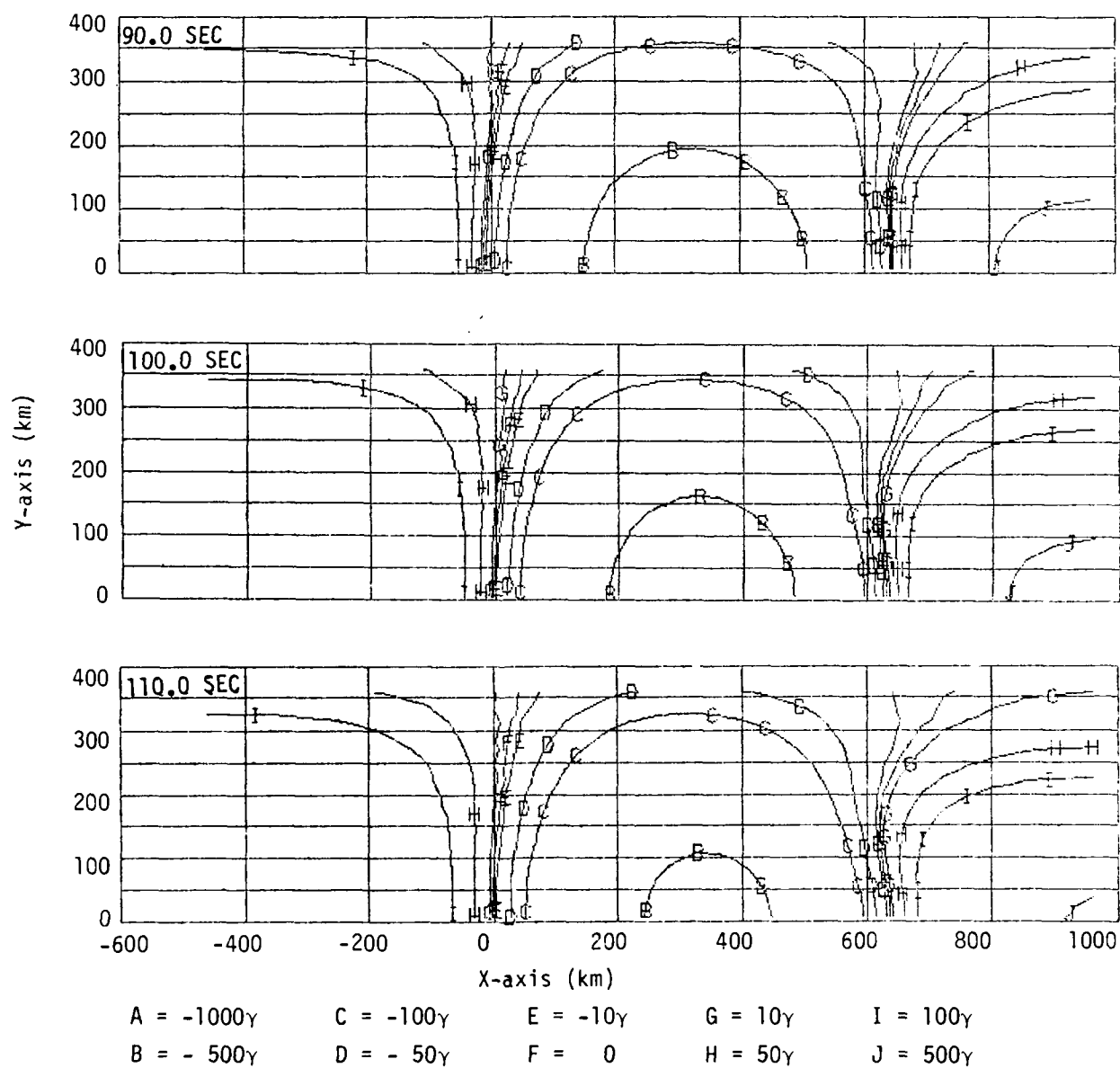
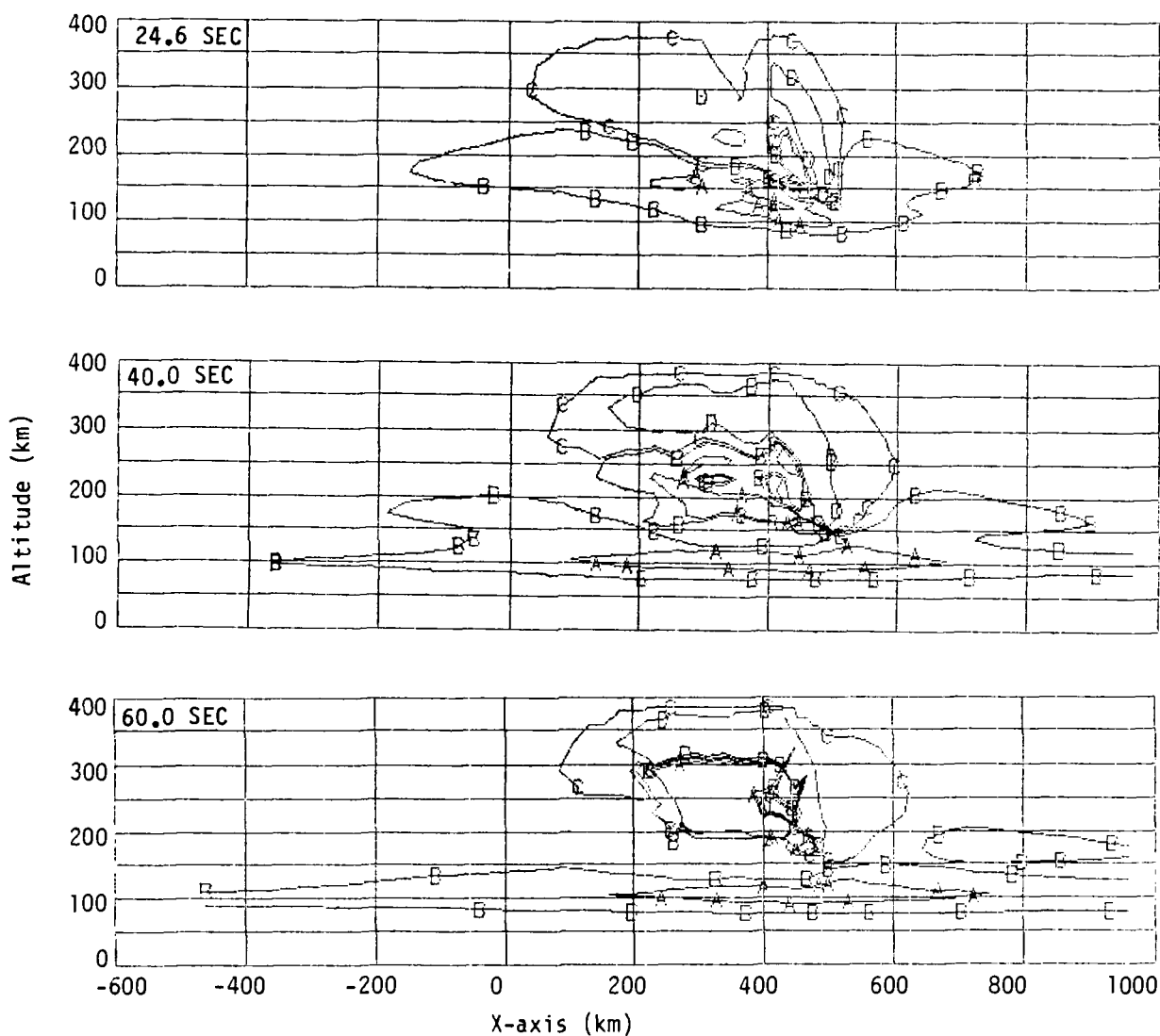
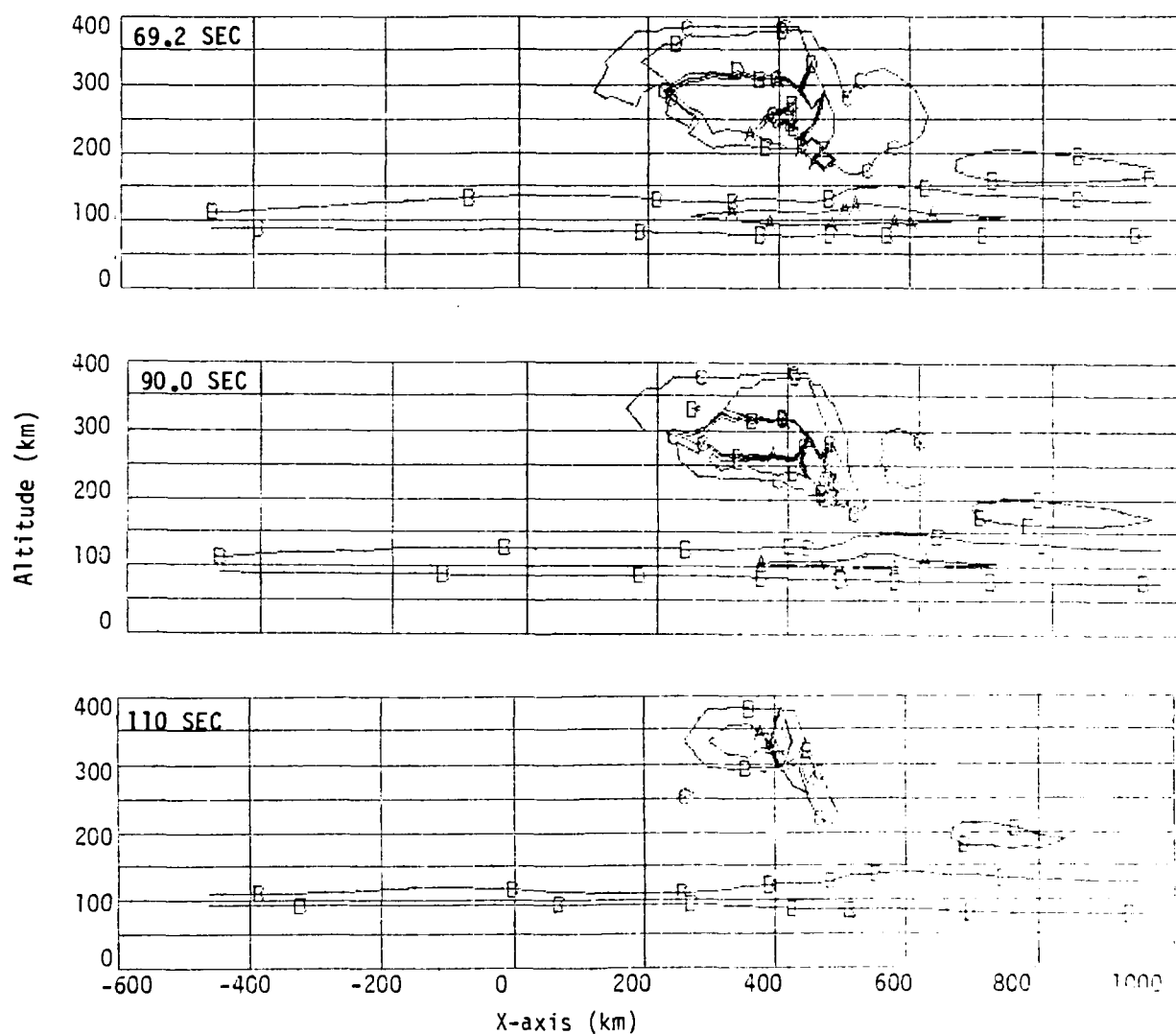


Figure 7.  $|\Delta \vec{B}|$  on the ground at 90.0, 100.0, 110.0 seconds. MICE  $N_e$  without beta patch.



$A = -10^{-9}$  abamps/cm<sup>2</sup> (Eastward)     $C = +10^{-10}$  abamps/cm<sup>2</sup> (Westward)  
 $B = -10^{-10}$  abamps/cm<sup>2</sup> (Eastward)     $D = +10^{-9}$  abamps/cm<sup>2</sup> (Westward)

Figure 8.  $\vec{j}_y$  in the symmetry plane at 24.6, 40.0, 60.0 seconds.  
MICE  $N_e$  without beta patch.



$A = -10^{-9}$  abamps/cm<sup>2</sup> (Eastward)     $C = +10^{-10}$  abamps/cm<sup>2</sup> (Westward)  
 $B = -10^{-10}$  abamps/cm<sup>2</sup> (Eastward)     $D = +10^{-9}$  abamps/cm<sup>2</sup> (Westward)

Figure 9.  $\vec{J}_y$  in the symmetry plane at 69.2, 90.0, 110.0 seconds.  
 MICE  $N_e$  without beta patch.

a conducting plane, the current tends to spread out as it flows east. At 40 seconds it is evident that significant current is flowing into the symmetry plane at a point further south than any of the significant generator currents. By 69.2 seconds this level of current extends to the southern edge of the grid, and at the same time the magnitude of the northern load currents have noticeably diminished in the region  $100 \text{ km} < x < 700 \text{ km}$ .

The strength of the southern return currents appears to increase slightly during the run compared to the northern return currents. The pattern of  $\Delta|\vec{B}|$  on the ground also shifts slightly to the south. Inspection of Figures 5 to 7 shows this to be the case. It is not a dramatic change, but the southern node line shifts from  $x = 100 \text{ km}$  to  $x = 0 \text{ km}$  from 40 seconds to 69.2 seconds. This shift does have a significant effect for magnetometers operating at or around J.I. Ten observer points were chosen along the symmetry plane for time plots of  $\Delta|\vec{B}|$ . Figure 10 is for an observer at  $x = -184 \text{ km}$ . The wiggles in the time plot are artificial electromagnetic waves in the lower atmosphere bouncing off of the side walls of the grid and are not real. We have varied the conductivities in the lower atmosphere and the dielectric constant and verified that these waves do not alter the mean  $\Delta|\vec{B}|$ . The observer at  $x = -184 \text{ km}$  always sees a  $|\vec{B}|$  greater than ambient consistent with the fact that the node line does not drift this far south. Figure 11 shows  $\Delta|\vec{B}|$  for an observer at  $x = 23.4 \text{ km}$ , the closest observer to J.I. The node passes through this point giving an early positive signal followed by a negative signal. This is the correct sequence of events, but the comparison to actual data is poor. Figure 12 shows the next observer at  $x = 179.2 \text{ km}$  north. This observer is always north of the node and sees a negative signal, which is an amazingly good fit to the J.I. data. The excellence of the fit can not be taken totally seriously, since our input data is not expected to have better than a factor of two type accuracy and perhaps is worse considering a new MICE Starfish is being planned. Taking Figures 11 and 12 together indicates that the MHD EMP code probably handles the essential details correctly.

X = - 184 KM  
NO BETA PATCH ALL SIDES AMBIENT

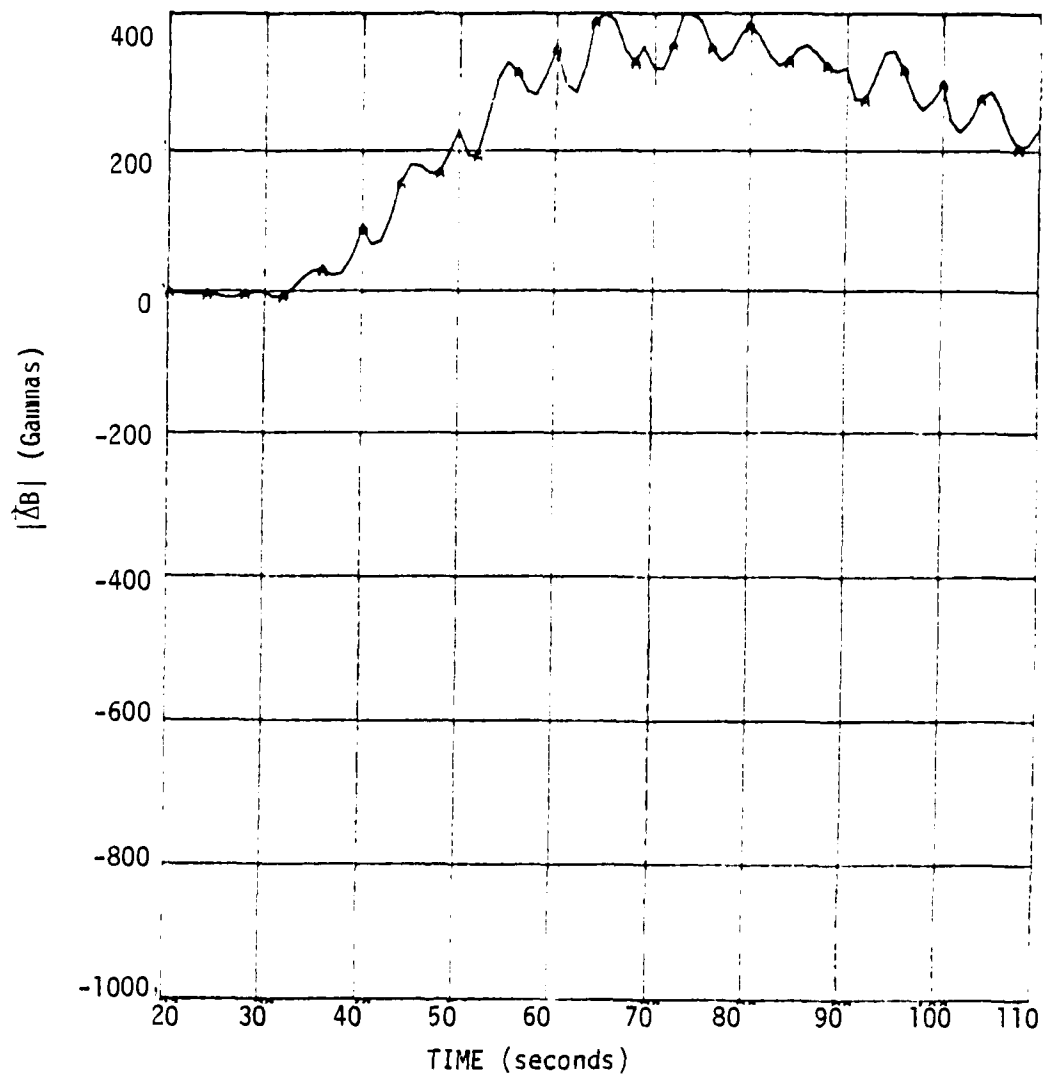


Figure 10.  $\Delta|\vec{B}|$  for an observer located at (x = -184 km, y=0).

X = 23.4 KM  
NO BETA PATCH ALL SIDES AMBIENT

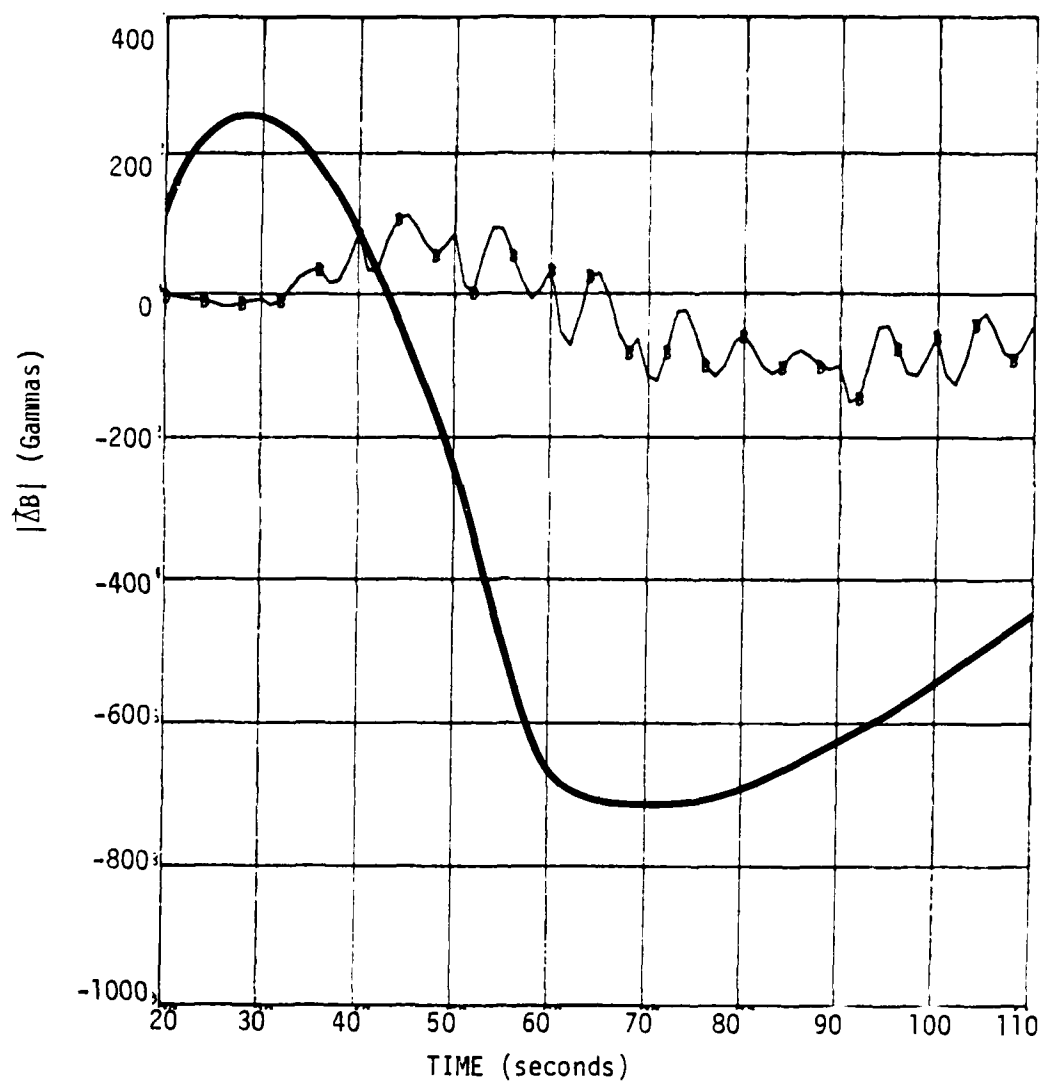


Figure 11.  $|\Delta \vec{B}|$  for an observer located at  $(x = 23.4 \text{ km}, y=0)$ .  
Smooth curve is experimental data for J.I.

X = 179.2 KM  
NO BETA PATCH ALL SIDES AMBIENT

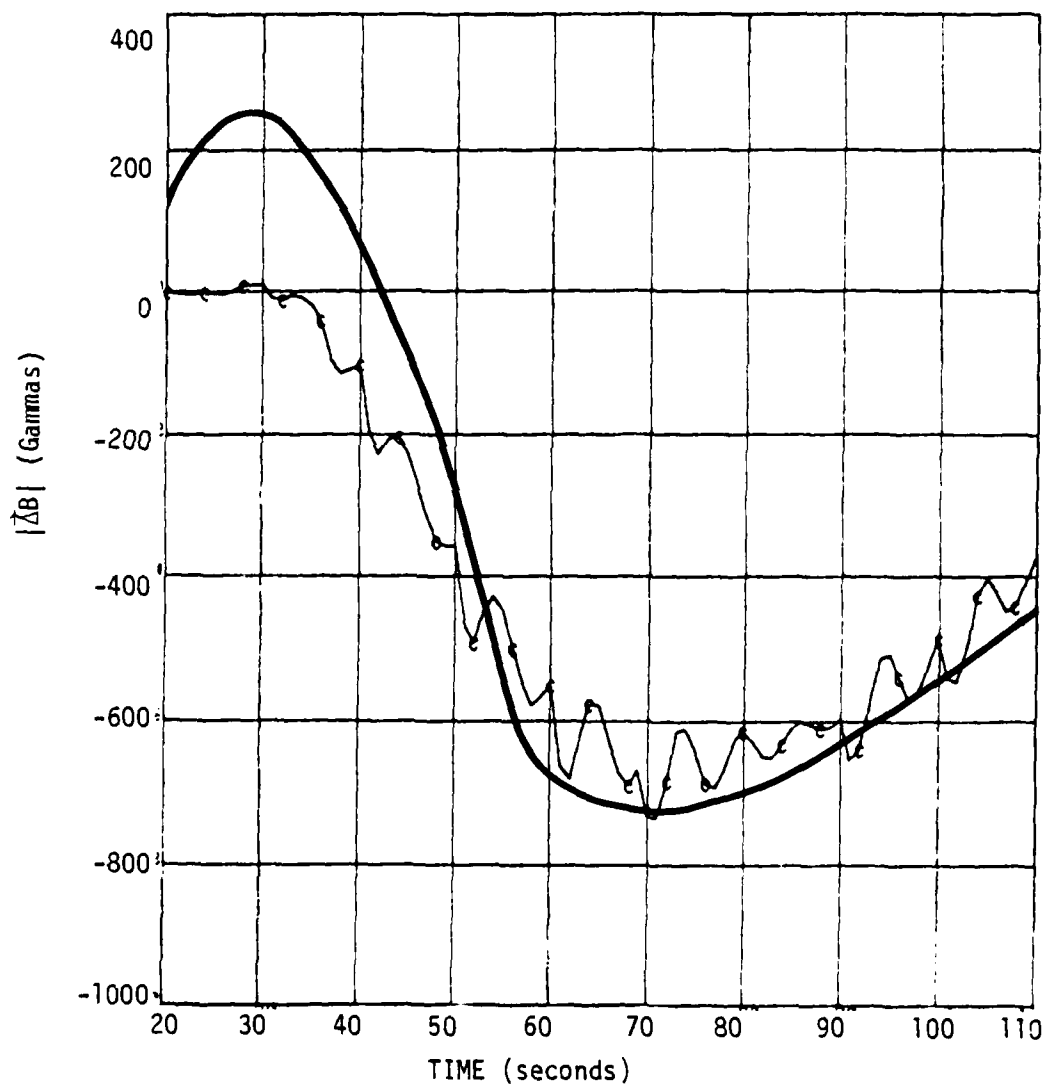


Figure 12.  $|\Delta \vec{B}|$  for an observer located at  $(x = 179.2 \text{ km}, y=0)$ .  
Smooth curve is experimental data for J.I.

We have only discussed the two load regions at 100 km altitude and have ignored the generator region and the load region immediately below it. During the simulation the orientation of the generator and this load region changes and they both rise. This should also influence the change in the pattern of the field on the ground.

Our results show that J.I. is at a particularly critical location. The positive pulse followed by a negative pulse occurs only in a limited region on the ground. It would require extremely accurate input data to reproduce the correct magnitude and time of both the positive and negative pulses and have them located precisely at J.I.



#### SECTION 4

#### ADDITIONAL CALCULATIONS

This section describes the differences between the three MHDEMP simulations. The first simulation used the standard MICE plasma parameters as input and had a beta patch. The second simulation used a third of the MICE electron density (denoted by  $N_e/3$ ), but had the same beta patch as the first simulation. The third simulation used the MICE  $N_e$ , but omitted the beta patch. The third simulation was described in detail in the previous section.

It is not possible to get a clear picture of the large scale differences between the three runs from the  $\Delta|\vec{B}|$  observations around J.I., since J.I. is strongly influenced by the nearby presence of the node line. The first two runs have nearly identical time histories of  $\Delta|\vec{B}|$  at J.I., but are different at all other observer points. The field near J.I. appears to change dramatically during the runs, while the change to the overall  $\vec{\Delta B}$  pattern is just a slight shift to the south.

The peak  $\Delta|\vec{B}|$  on the ground is a simple measure of the important large scale differences between the runs, as well as being an important parameter for system EMP effects. The time, location and magnitude of the peak  $\Delta|\vec{B}|$  on the ground is shown in Table 1. The data in Table 1 is taken from the ten observer points on the symmetry plane. The first two runs have a beta patch and therefore have more conductivity between the kinetic energy patch of the nuclear burst and the ground than the third run. The third run without a beta patch showed that  $\Delta|\vec{B}|$  peaked earlier

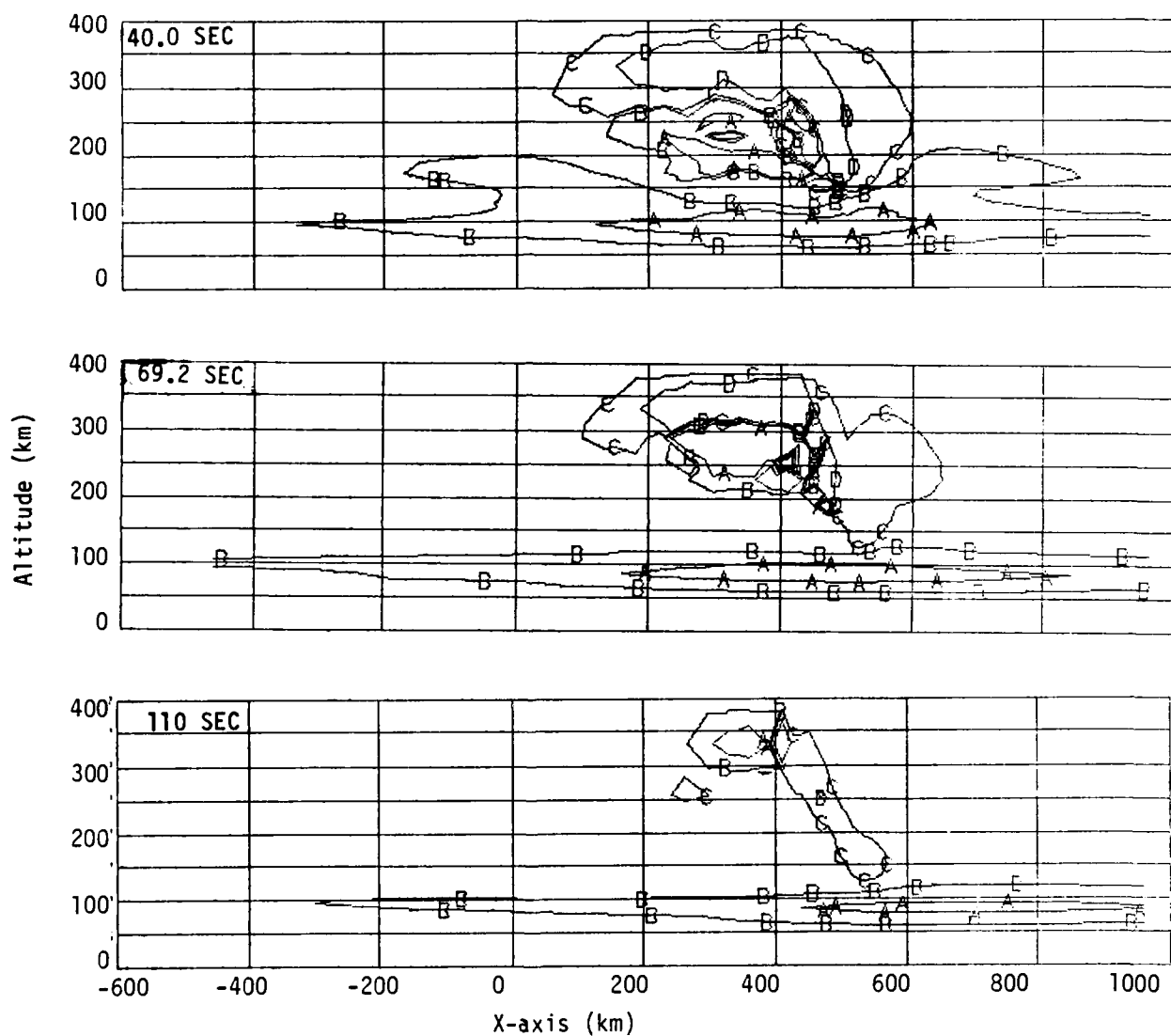
Table 1. Comparison of peak signal on ground.

	Peak $\Delta \vec{B} $	Time	Location
1. Standard MICE $N_e$ Standard Beta Patch	-700 $\gamma$	110 seconds	x = 300 km
2. MICE $N_e/3$ Standard Beta Patch	-580 $\gamma$	110 seconds	x = 300 km
3. Standard MICE $N_e$ No Beta Patch	-950 $\gamma$	70 seconds	x = 380 km

since the magnetic diffusion time to the ground was shorter due to the lesser conductivity. The magnitude of  $\Delta|\vec{B}|$  for the third run was greater since there was less shielding by the conductivity.

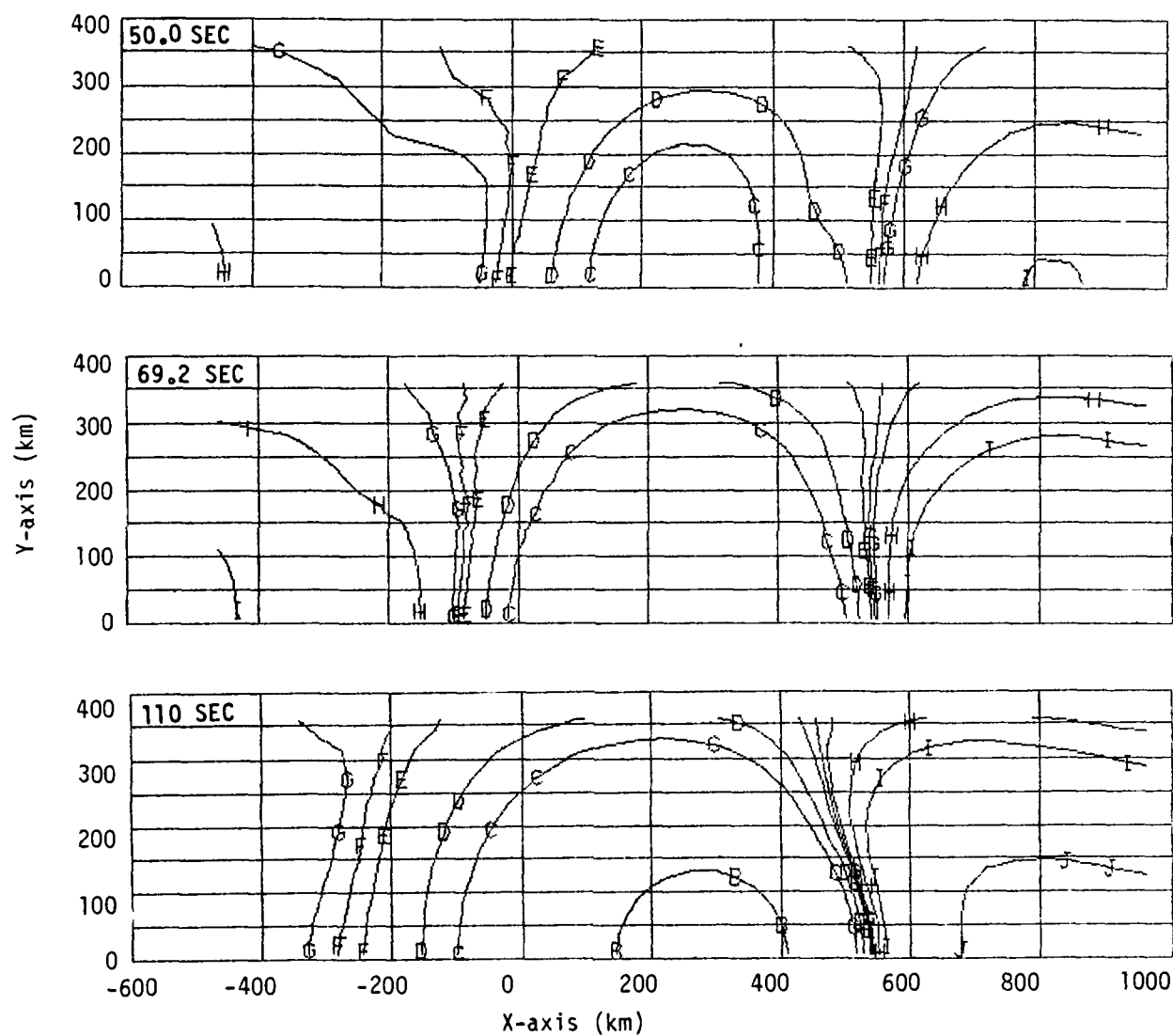
As expected, the second run with only one-third of the MICE  $N_e$  had less current in the generator region and therefore the smallest signal on the ground. The computed variation in the magnitude of the peak  $\Delta|\vec{B}|$  among the three runs is smaller than one might have expected.

The location of the peak  $\Delta|\vec{B}|$  occurred farther to the south for the first two runs. The beta patch increases the conductivity more in the northern load region than in the southern load region. Figure 13 shows the load and generator currents for the standard MICE  $N_e$  run with the beta patch. At 40 and 69.2 seconds the return currents in the conducting plane appear to be just as spread out, if not more so, as those in the run without the beta patch shown in Figures 8 and 9. At 110 seconds the return currents have shifted to the north. This run had the same two ring current patterns on the ground and Figure 14 shows that the southern



A =  $-10^{-9}$  abamps/cm<sup>2</sup> (Eastward)    C =  $+10^{-10}$  abamps/cm<sup>2</sup> (Westward)  
 B =  $-10^{-10}$  abamps/cm<sup>2</sup> (Eastward)    D =  $+10^{-9}$  abamps/cm<sup>2</sup> (Westward)

Figure 13.  $J_y$  in the symmetry plane for model with the standard MICE  $N_e$  and a beta patch at 40.0, 69.2, 110.0 seconds.

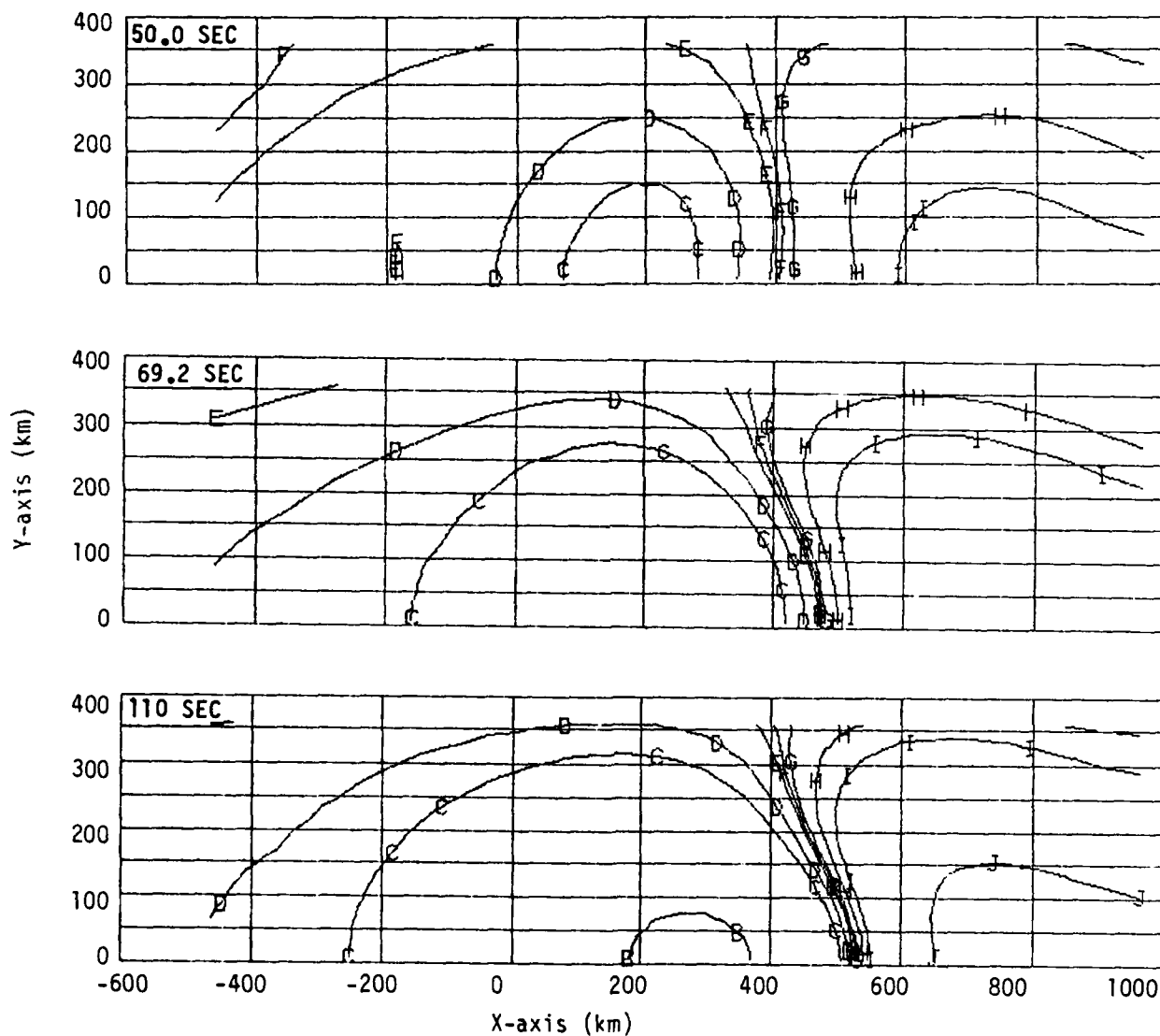


A =  $-1000\gamma$     C =  $-100\gamma$     E =  $-10\gamma$     G =  $10\gamma$     I =  $100\gamma$   
 B =  $-500\gamma$     D =  $-50\gamma$     F = 0    H =  $50\gamma$     J =  $500\gamma$

Figure 14.  $\Delta|\vec{B}|$  on the ground for model with the standard MICE  $N_e$  and a beta patch at 50.0, 69.2, 110.0 seconds.

node line drifted south more than in the run without the beta patch. The fact that the node moved south can not be associated with the current pattern in the E-layer shifting south, since they went north. At 110 seconds the southern current loop on the ground is practically gone.

The  $N_e/3$  run had insignificant current in the southern load region and only had one current ring on the ground and only the northern node line. Figure 15 shows  $\Delta|\vec{B}|$  on the ground for the  $N_e/3$  run.



$A = -1000\gamma$      $C = -100\gamma$      $E = -10\gamma$      $G = 10\gamma$      $I = 100\gamma$   
 $B = -500\gamma$      $D = -50\gamma$      $F = 0$      $H = 50\gamma$      $J = 500\gamma$

Figure 15.  $\Delta|\vec{B}|$  on the ground for model with one-third of the MICE  $N_e$  and a beta patch at 50.0, 69.2, 110.0 seconds.

## SECTION 5

### CONCLUSIONS AND POSSIBLE FUTURE IMPROVEMENTS

Some questions are still to be resolved. We only had one current loop for the  $N_e/3$  run. We are not sure exactly why the  $\Delta|\vec{B}|$  pattern drifts south during the run. It is probably related to the geometry of the currents changing as the generator region gains altitude. The model without the beta patch gives a better fit to the J.I. data than the beta patch model. The better fit may be accidental.

The symmetry breaking Hall term should be incorporated into the MHDEMP code on an experimental basis. It should make a difference in the load region near 100 km altitude. Our beta patch model may be too rough, since we are using 8 km grid spacings in altitude. It may be that we are overestimating the beta patch  $N_e$  or the effective beta patch conductivities may be less than imagined due to irregularities in electron density caused by early time instabilities in the debris-air mixing. The beta patch was observed to be irregular. The effective conductivity through the beta patch should be derived by averaging the resistivities along the current path. This would lead to a smaller effective conductivity than our smooth distribution of beta patch electrons.

Forcing the currents to close inside the MICE grid may affect the fine features of the  $\Delta\vec{B}$  pattern on the ground, such as the precise location of the node line. This is true for the currents in the E-layer, since this region extends around the world. Currents in the kinetic energy patch appear far enough away from the boundaries. If more accuracy is desired, the MHDEMP grid could be expanded beyond the MICE grid. The plasma para-

meters are updated only at MICE dump times, which are spaced 15 seconds apart by the end of the simulation. Better accuracy could be obtained by interpolating the parameters in time and updating more often. This would also decrease the magnitude of the artificial electromagnetic waves in the lower atmosphere which are responsible for the wiggles in Figures 10 to 12. These waves are excited whenever the plasma parameters are updated. Future MHDEMP simulations should be started at earlier times than 20 seconds to reproduce the positive signal. In that case it may be worthwhile to include the pressure gradient as well as the neutral slip as MICE does. These simulations were started at 20 seconds since we originally were concentrating on the late time negative signal.

In summation, the MHDEMP code working with MICE input data reproduced the general features of the Starfish data. We are now ready to use other existing MICE runs with various yields and burst altitudes to determine which bursts produce the greatest magnetohydrodynamic EMP effects on long-line systems.



## REFERENCES

1. Messier, M. A., R. W. Kilb, and C. L. Longmire, Magnetohydrodynamic EMP, Unpublished.
2. Messier, M. A., and J. Harberger, MHD EMP Revisited, Unpublished.
3. Harberger, J. H., R. W. Kilb, and C. L. Longmire, Burst Region and Remote Current Sources Contributing to MHD-EMP, Unpublished.
4. Longmire, C. L., DNA Briefing prepared for Capt. Mike Bell, DNA/RAEV.
5. Fajen, F. E., MICE: An Implicit Difference Scheme for MHD Calculations, DNA 2877Z, Mission Research Corporation, March 1973.
6. Physics of High-Altitude Nuclear Burst Effects, DNA 4501F, Mission Research Corporation, December 1977. (See Equations 12-135 and 12-136.)
7. Boris, J., A Physically Motivated Solution of the Alfven Problem, NRL Memo Report 2167, Naval Research Laboratory, November 1970.
8. Longmire, C. L., Debris-Air Mixing and Beta Ray Aurorae, Unpublished.

APPENDIX  
THE MAGNETOHYDRODYNAMIC EMP  
BRIEFING PREPARED FOR CAPT. MIKE BELL, DNA (RAEV)  
BY  
CONRAD L. LONGMIRE, MRC  
October 1978

1. HIGH-ALTITUDE NUCLEAR EXPLOSIONS GENERATE ELECTROMAGNETIC FIELD (OR EMP) THROUGH SEVERAL PROCESSES.

1.1 GAMMA RAYS → CURRENTS OF COMPTON RECOIL ELECTRONS → EM FIELDS.

GAMMA INDUCED EMP IS LARGE FOR ABOUT 1  $\mu$ SEC, THEN FALLS OFF. SEEN BY OBSERVERS FROM GROUND LEVEL UP.

THIS IS THE MOST WELL KNOWN MECHANISM.

THEORY ESTABLISHED IN 1964.

COMPUTER CODES: CHAP AND HEMP B FOR EARLY TIMES, LHAP AND HAPS FOR LATE TIMES.

CALCULATIONS ARE IN GOOD AGREEMENT WITH EXPERIMENTAL DATA FROM OPERATION FISHBOWL.

1.2 X RAYS → PHOTOELECTRONS → EM FIELDS.

THIS EFFECT IS PRIMARILY A NON-PROPAGATING PLASMA OSCILLATION, SEEN IN THE REGION ABOVE 50-KM ALTITUDE WHERE X RAYS ARE ABSORBED, BELIEVED INSIGNIFICANT FOR LOWER OBSERVERS.

SOME THEORY. CODES: XEMP, PEMP.

1.3 NEUTRONS → COLLISIONS WITH AIR ATOMS → GAMMA RAYS → EM FIELDS.

SPEED OF FASTEST NEUTRONS  $\approx$  50 KM/MILLISEC.

THIS EFFECT IMPORTANT IN MILLISECOND TIME FRAME.

NO THEORY. CODE: HAPS; COULD BE INCLUDED IN LHAP.

1.4 (HYDRODYNAMIC MOTIONS)  $\times$  (GEOMAGNETIC FIELD) → EMF → CURRENTS IN SURROUNDING PLASMA → MAGNETIC FIELD PERTURBATIONS.

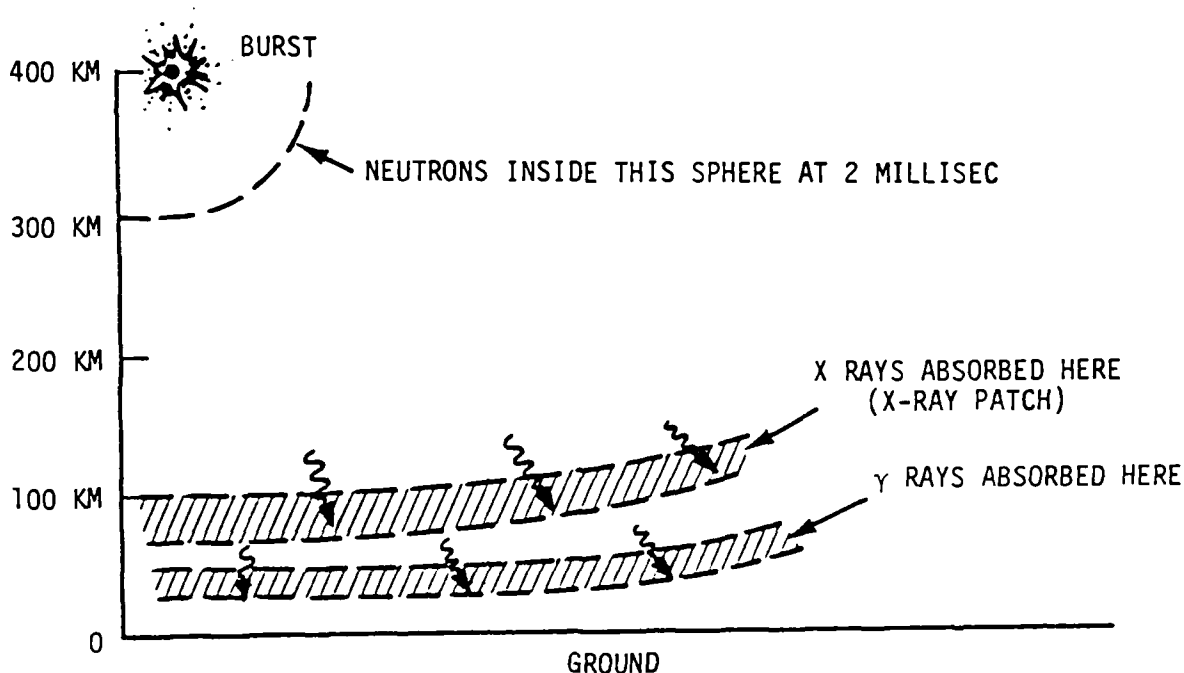
THESE EFFECTS ARE CALLED MHD EMP.

IMPORTANT FOR LONG-LINE GROUND SYSTEMS.

TIME FRAME: TENS TO HUNDREDS OF SECONDS.

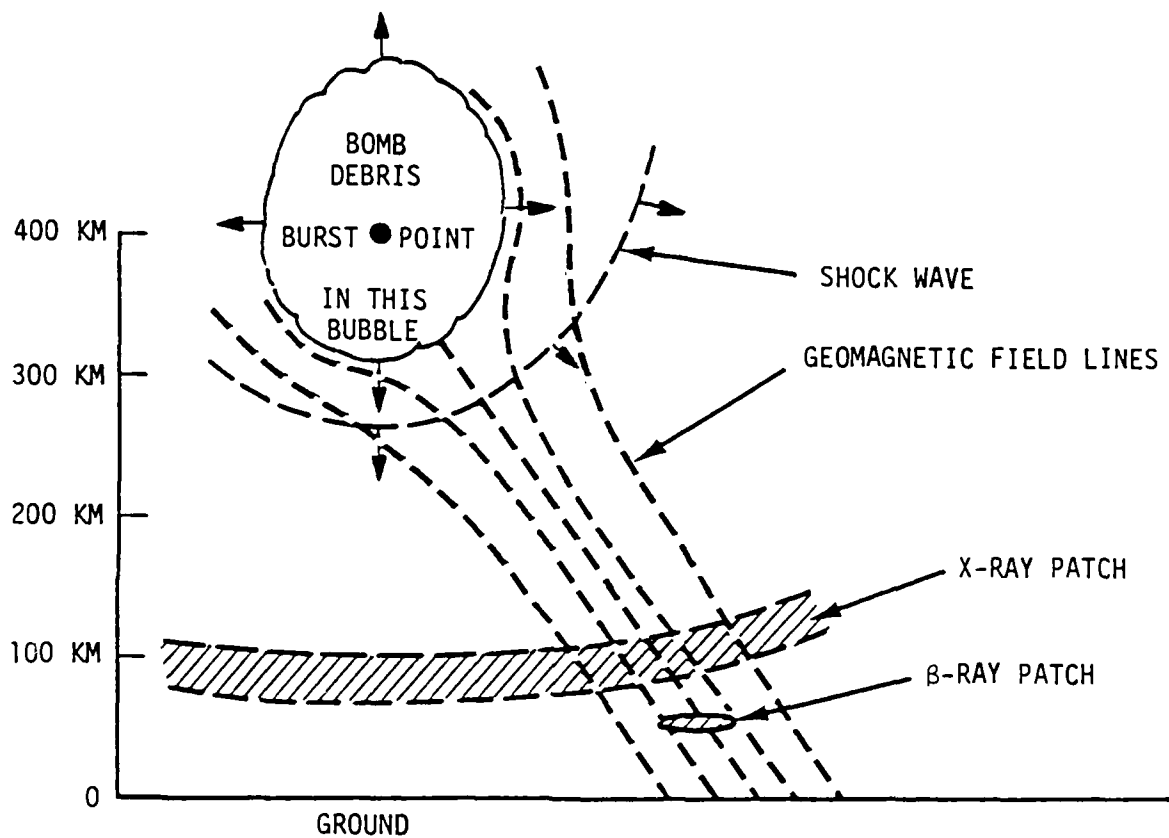
## 2. SEQUENCE OF EVENTS RELEVANT TO MHD EMP

### 2.1 $T \approx$ FEW MILLISEC



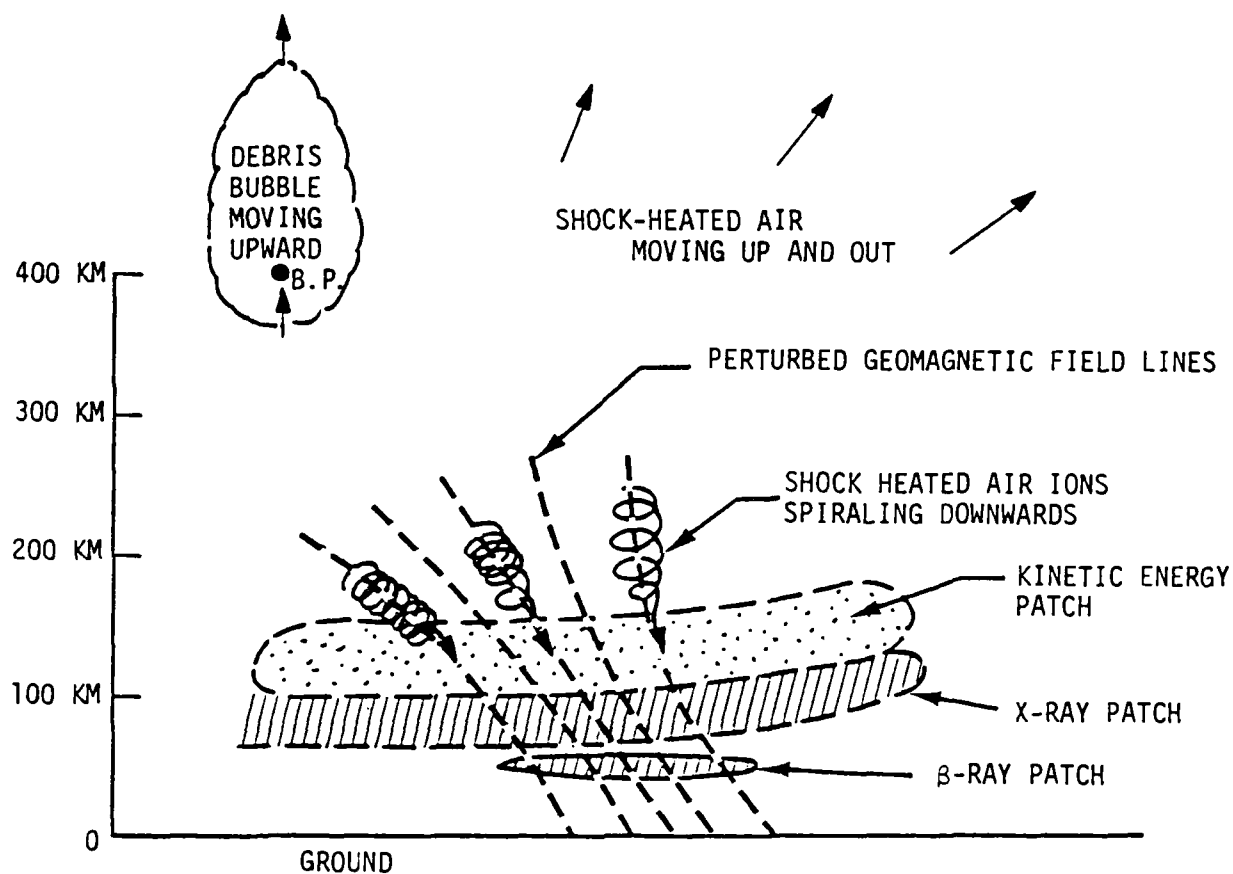
- GAMMA RAYS ABSORBED BETWEEN 20 AND 50 KM.  
MAKE EMP, DURATION  $\sim 1 \mu$  SEC. INDUCED CONDUCTIVITY DIES AWAY IN 0.1 TO 1 MILLISEC.
- X RAYS ABSORBED BETWEEN 70 AND 100 KM.  
MAKE PLASMA OSCILLATIONS. INDUCED CONDUCTIVITY LINGERS FOR  $\approx 10$  SEC, SCREENS GROUND OBSERVERS FROM EARLY PART OF MHD EMP.

2.2  $T \approx 0.1$  SEC



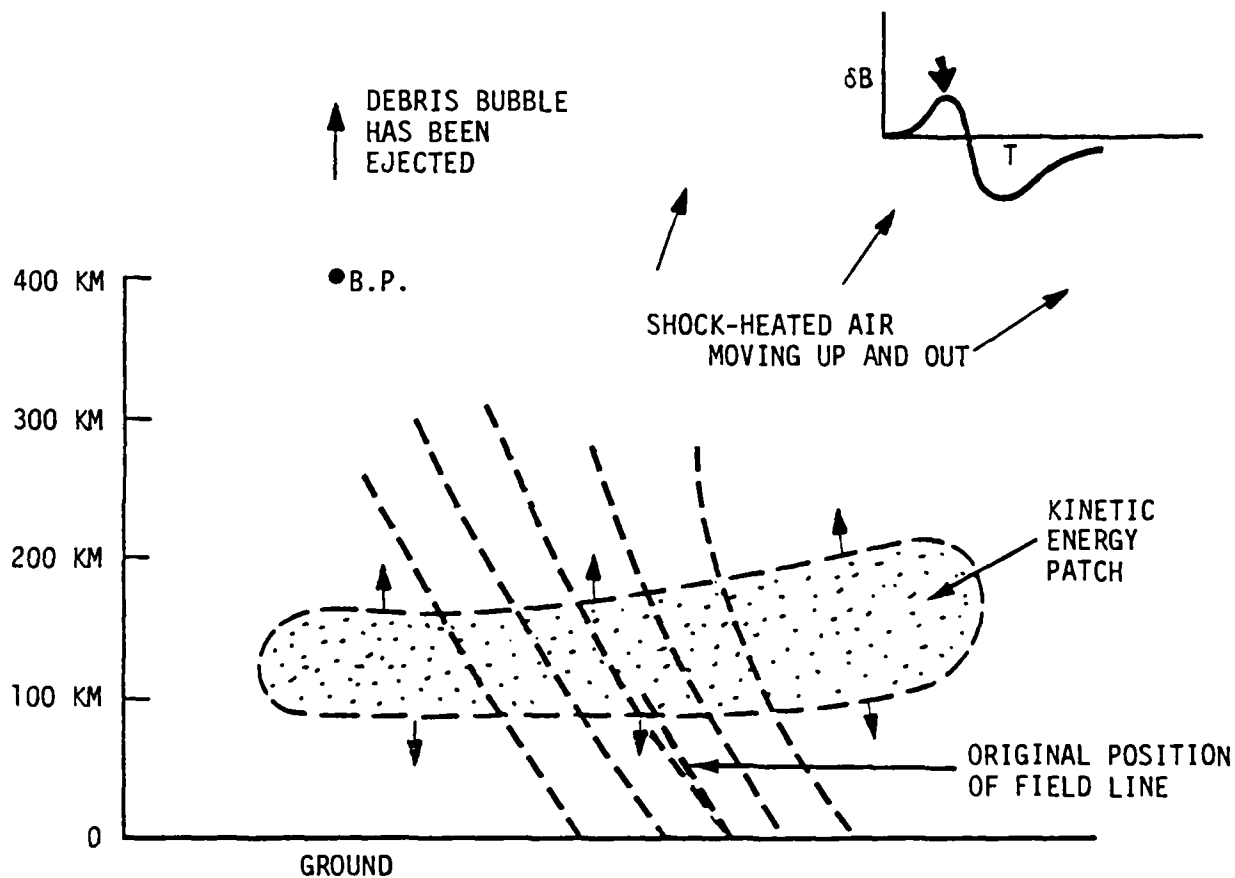
- EXPANDING BOMB DEBRIS AND SHOCK WAVE PUSH GEOMAGNETIC FIELD AWAY FROM BURST REGION.
- GEOMAGNETIC PERTURBATIONS SCREENED FROM GROUND OBSERVERS BY CONDUCTING X-RAY PATCH.
- SHOCK WAVE HEATS A LARGE VOLUME OF THE UPPER ATMOSPHERE.
- $\beta$ -RAY PATCH COULD MAKE MAGNETIC PERTURBATIONS. PROBABLY SMALL; NO EXPERIMENTAL DATA.

2.3  $T \approx 1 \text{ SEC}$



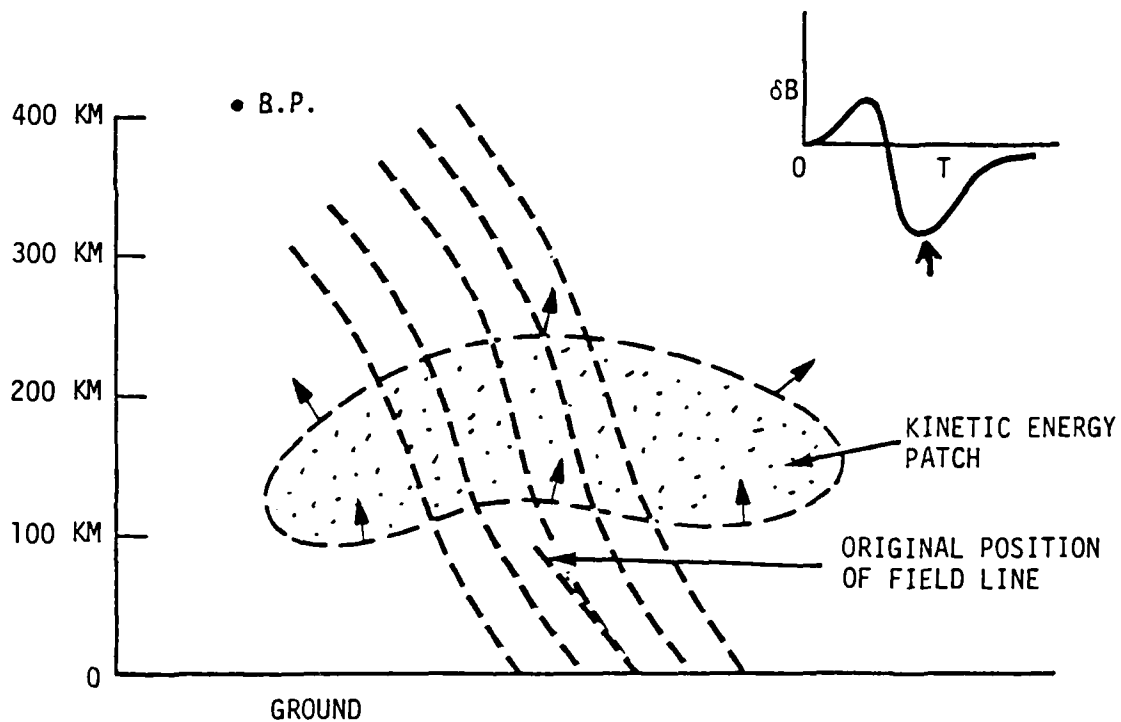
- BOMB DEBRIS AND SHOCK-HEATED AIR AT HIGH ALTITUDES MOVE UPWARDS AND OUTWARDS, CARRYING GEOMAGNETIC FIELD ALONG, CAUSING VERY LARGE GEOMAGNETIC FIELD DISTORTIONS.
- THESE PERTURBATIONS STILL SCREENED FROM GROUND OBSERVERS BY CONDUCTIVITY IN X-RAY PATCH.
- SHOCK-HEATED AIR IONS AT LOWER ALTITUDES SPIRAL DOWN FIELD LINES, ARE STOPPED IN AIR BETWEEN 100 AND 150 KM, CREATE KINETIC ENERGY PATCH (SOMETIMES CALLED DEBRIS PATCH).

2.4  $T \approx 20$  SEC



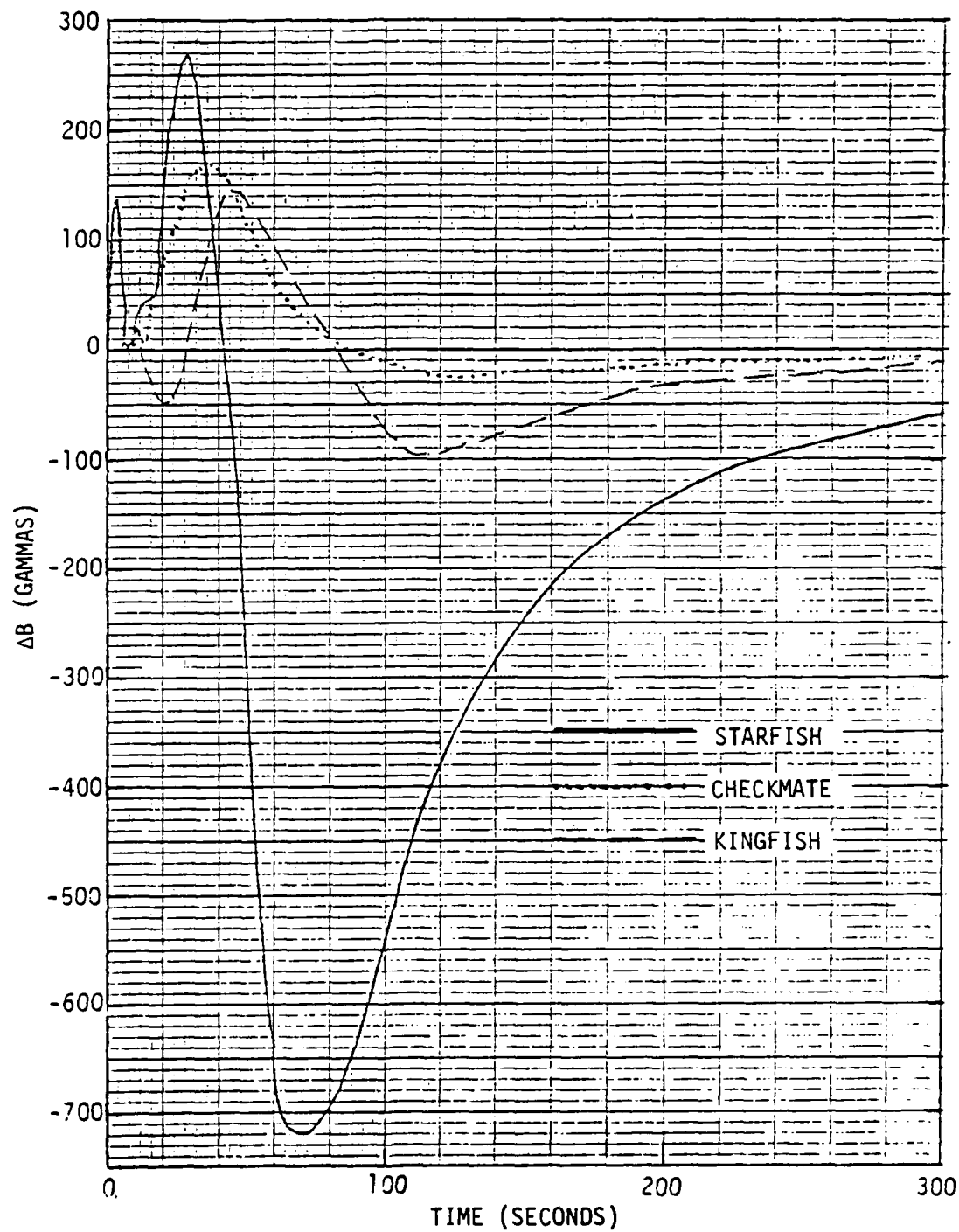
- CONDUCTIVITY IN X-RAY PATCH IS GONE BY RECOMBINATION.
- BOTTOM OF KINETIC ENERGY PATCH EXPANDS DOWNWARD, COMPRESSING HORIZONTAL COMPONENT OF GEOMAGNETIC FIELD AGAINST EARTH.
- TOP OF KINETIC ENERGY PATCH EXPANDS UPWARDS BUT THIS EFFECT IS SCREENED FROM GROUND OBSERVERS BY CONDUCTIVITY IN PATCH.

2.5  $T \approx 100$  SEC



- ENTIRE KINETIC ENERGY PATCH EXPANDS AND RISES, TENDING TO CARRY GEOMAGNETIC FIELD WITH IT.
- HORIZONTAL COMPONENT OF FIELD BETWEEN PATCH AND GROUND IS EXPANDED AND REDUCED.

### 3. EXPERIMENTAL DATA

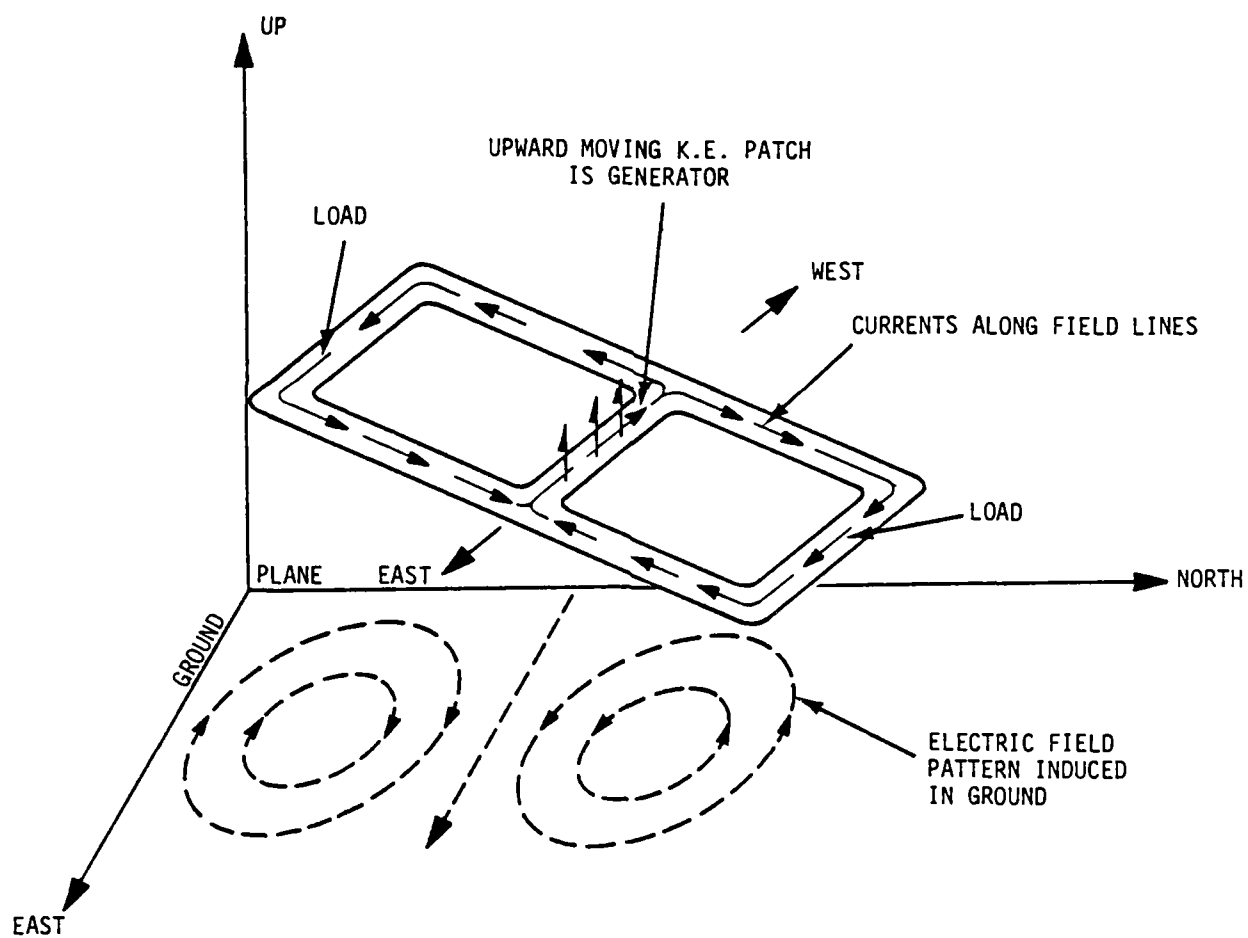


MAGNETOMETER DATA FROM JOHNSTON ISLAND  
FOR FISHBOWL DATA TESTS

1 GAMMA =  $10^{-5}$  GAUSS



#### 4. ELECTRIC FIELD PATTERNS



- UPWARD MOVING K.E. PATCH (HEAVE) GENERATES EAST-WEST EMP.
- CURRENTS FLOW ALONG MAGNETIC FIELD LINES TO LOADS OUTSIDE K.E. PATCH.
- CURRENTS MAKE CHANGES IN MAGNETIC FIELD WHICH INDUCE ELECTRIC FIELDS IN GROUND.

5. FIELD MAGNITUDES EXPECTED

- STARFISH 8B AT JOHNSTON ISLAND WAS -700 GAMMAS.  
FIELD CHANGE WAS PROBABLY CONSIDERABLY LARGER NORTH OF J.I.
- 700 GAMMAS  $\longrightarrow$   $E \approx 0.05$  VOLTS/KM IN OCEAN  
 $E \approx 3$ . VOLTS/KM IN LAND
- MRC HAS SUGGESTED THAT E MAY BE AS LARGE AS 30 VOLTS/KM FOR SINGLE BURST, 100 VOLTS/KM FOR MULTIPLE BURSTS WITHIN 100 SECOND INTERVAL.
- BASIS FOR THESE ESTIMATES IS EXCEEDINGLY SHAKY AT PRESENT.
- SIZE OF GROUND AREAS EXPOSED IS SEVERAL HUNDRED KILOMETERS.

## 6. VULNERABILITY MECHANISMS

- PRIMARILY OF CONCERN FOR LONG-LINE SYSTEMS.
- COPPER WIRE WITH  $1 \text{ cm}^2$  CROSS SECTION, 100 KM LONG HAS  $R \approx 17 \text{ OHMS}$ , SEES VOLTAGE 3000 VOLTS. IF GROUNDED AT BOTH ENDS, CURRENT  $\approx 180 \text{ AMPS}$  FOR 100 SECONDS. HEAT DEVELOPED  $\approx 5 \text{ JOULE/CM}^3$ ; TEMPERATURE RISE  $\approx 1.5^\circ\text{C}$ . NOT BAD.
- IF COMPARABLE TOTAL ENERGY ( $10^7 \text{ JOULES}$ ) WERE DUMPED INTO A PROTECTIVE DEVICE AT ONE END OF THE WIRE, IT COULD BE SERIOUS.
- IN TYPICAL LONG-LINE COMMUNICATIONS SYSTEMS THE WIRE IS NOT GROUNDED (TO PREVENT TELLURIC CURRENTS). THEN 3000 VOLTS APPEARS BETWEEN EQUIPMENT AND GROUND. MANY SYSTEMS THEN TURN THEMSELVES OFF. IN SOME SYSTEMS, D.C. CURRENT THROUGH WIRE, WITH GROUND RETURN, IS USED TO POWER REPEATERS. THESE MUST BE TURNED OFF. MAGNETIC STORMS COMMONLY CAUSE SUCH OUTAGES.

## DISTRIBUTION LIST

### DEPARTMENT OF DEFENSE

Assistant to the Secretary of Defense  
Atomic Energy

ATTN: Executive Assistant

Defense Communications Agency

ATTN: Code 312

ATTN: Code C313

Defense Communications Engineer Center

ATTN: Code R123

ATTN: Code R400

ATTN: Code R720, C. Stansberry

Defense Intelligence Agency

ATTN: RDS-3A

ATTN: DB 4C2, D. Spohn

Defense Nuclear Agency

2 cy ATTN: RAEE

4 cy ATTN: TITL

Defense Technical Information Center

12 cy ATTN: DD

Field Command

Defense Nuclear Agency

ATTN: FCP

ATTN: FCLMC

Field Command

Defense Nuclear Agency

Livermore Branch

ATTN: FCPRL

Interservice Nuclear Weapons School

ATTN: TTV

Joint Chiefs of Staff

ATTN: J-3

Joint Strat Tgt Planning Staff

ATTN: NRI STINFO, Library

ATTN: JLA

ATTN: JPST

ATTN: JSAS

National Communications System

ATTN: NCS-TS

Under Secretary of Defense for Rsch & Engrg

ATTN: Strategic & Space Sys (OS)

### DEPARTMENT OF THE ARMY

BMD Systems Command

Department of the Army

ATTN: BMDSC-HW, R. DeKalb

ATTN: BMDSC-HLE, R. Webb

ATTN: BMDSC-AOLIB

Electronics Tech & Devices Lab

U.S. Army Electronics R&D Command

ATTN: DELSD-L, W. Werk

ATTN: DELCS-K, A. Cohen

ATTN: DRDCO-COM-ME, G. Gaulle

### DEPARTMENT OF THE ARMY (Continued)

Harry Diamond Laboratories

Department of the Army

ATTN: DELHD-N-EMC

ATTN: DELHD-N-EM

ATTN: NWPO

ATTN: DELHD-N-TD

ATTN: DELHD-N-EMB

ATTN: DELHD-I-TL

ATTN: DELHD-N-TF

ATTN: DELHD-N-EMD

ATTN: DELHD-N-EME

ATTN: DELHD-N-RB

ATTN: DELHD-N-EMA

U.S. Army Comm-Elec Engrg Instal Agency

ATTN: CCC-CED-SES

U.S. Army Communications Command

ATTN: ATSI-CD-MD

ATTN: CC-OPS-OS

ATTN: CC-OPS-PD

U.S. Army Electronics R&D Command

ATTN: DRDCO-SEI

ATTN: DRCPM-ATC

U.S. Army Engineer Div, Huntsville

ATTN: HNDED-SR

U.S. Army Intel Threat Analysis Detachment

ATTN: Admin Officer

U.S. Army Intelligence & Sec Cmd

ATTN: Technical Library

ATTN: Tech Info Fac

U.S. Army Materiel Sys Analysis Actvty

ATTN: DRXSY-PO

### DEPARTMENT OF THE NAVY

Naval Electronic Systems Command

ATTN: PME 117-21

Naval Ocean Systems Center

ATTN: Code 7309, R. Greenwell

Naval Postgraduate School

ATTN: Code 1424, Library

Naval Research Laboratory

ATTN: Code 6623, R. Statler

ATTN: Code 2627, D. Folen

ATTN: Code 1434, E. Brancato

ATTN: Code 6624

Naval Surface Weapons Center

ATTN: Code F32, E. Rathbun

ATTN: Code F30

Naval Surface Weapons Center

ATTN: Code F-56

DEPARTMENT OF THE NAVY

Strategic Systems Project Office  
Department of the Navy  
ATTN: NSP-2342, R. Coleman  
ATTN: NSP-2701, J. Pitsenberger  
ATTN: NSP-43  
ATTN: NSP-27334  
ATTN: NSP-230, D. Gold

DEPARTMENT OF THE AIR FORCE

Aeronautical Systems Division  
Air Force Systems Command  
ATTN: ASD/YEF  
ATTN: ASD/ENFTV  
ATTN: ASD/ENAMA, J. Corbin

Air Force Weapons Laboratory  
Air Force Systems Command

ATTN: CA  
ATTN: ELT, W. Page  
ATTN: EL, C. Baum  
ATTN: ELXT  
ATTN: SUL  
ATTN: NT  
ATTN: ELP  
ATTN: ELA, J. Castillo  
ATTN: NXS  
ATTN: NTN  
ATTN: M. Schneider

Air Logistics Command  
Department of the Air Force  
ATTN: OO-ALC/MMETH, P. Berthel  
ATTN: OO-ALC/MMEDO, L. Kidman

Air University Library  
Department of the Air Force  
ATTN: AUL-LSE

Ballistic Missile Office  
Air Force Systems Command  
ATTN: ENSN, J. Allen

Electronic Systems Division  
ATTN: YSEA

Foreign Technology Division  
Air Force Systems Command  
ATTN: TQTD, B. Ballard  
ATTN: NIIS, Library

Headquarters Space Division  
Air Force Systems Command  
ATTN: IND

Headquarters Space Division  
Air Force Systems Command  
ATTN: YLPC

Northern American Air Defense Treaty  
ATTN: JSYE, P. Castleberry

Strategic Air Command  
Department of the Air Force  
ATTN: XPFS, F. Tedesco  
ATTN: NRI STINFO, Library  
ATTN: DEL

DEPARTMENT OF ENERGY

Department of Energy  
Economic Regulatory Administration  
ATTN: Office of Utility Systems, L. O'Neill

OTHER GOVERNMENT AGENCIES

Central Intelligence Agency  
ATTN: OSWR/NED

Federal Emergency Management Agency  
National Sec Ofc Mitigation & Rsch  
ATTN: Plans & Operations (SE)  
ATTN: Plans & Operations (EO)

Federal Preparedness Agency  
General Services Administration  
ATTN: ESTE, M. Murtha

DEPARTMENT OF ENERGY CONTRACTORS

Lawrence Livermore National Lab  
ATTN: Technical Info Dept, Library  
ATTN: L-156, H. Cabayan  
ATTN: L-153, D. Meeker  
ATTN: L-96, T. Donich  
ATTN: L-10, H. Kruger  
ATTN: L-156, E. Miller

Los Alamos National Laboratory  
ATTN: B. Noel  
ATTN: MS 670, J. Hopkins  
ATTN: C. Benton

Sandia National Lab  
ATTN: R. Parker  
ATTN: C. Vittitoe  
ATTN: E. Hartman

DEPARTMENT OF DEFENSE CONTRACTORS

AVCO Research & Systems Group  
ATTN: Library A830

Battelle Memorial Institute  
ATTN: E. Leach

BDM Corp  
ATTN: Corporate Library

BDM Corp  
ATTN: Library

Bendix Corp  
ATTN: M. Frank

Bendix Corp  
ATTN: Dept 6401

Boeing Co  
ATTN: H. Wicklein  
ATTN: D. Kemle  
ATTN: V. Jones  
ATTN: B. Hanrahan  
ATTN: Kent Technical Library

Charles Stark Draper Lab, Inc  
ATTN: TIC MS 74  
ATTN: K. Fertig

DEPARTMENT OF DEFENSE CONTRACTORS (Continued)

Dikewood Corporation  
ATTN: Technical Library  
ATTN: L. Davis  
ATTN: C. Jones

Dikewood Corporation  
ATTN: K. Lee

Effects Technology, Inc  
ATTN: Technical Info Acq, S. Clow

EG&G Wash. Analytical Svcs Ctr, Inc  
ATTN: C. Giles

Electro-Magnetic Applications, Inc  
ATTN: D. Merewether

Franklin Institute  
ATTN: R. Thompson

Georgia Institute of Technology  
ATTN: R. Curry

Georgia Institute of Technology  
ATTN: H. Denny

IIT Research Institute  
ATTN: J. Bridges  
ATTN: I. Mindel

Institute for Defense Analyses  
ATTN: Tech Info Services

International Tel & Telegraph Corp  
ATTN: Technical Library  
ATTN: A. Richardson

JAYCOR  
ATTN: W. Radasky

Kaman Sciences Corp  
ATTN: N. Beauchamp  
ATTN: F. Shelton  
ATTN: A. Bridges  
ATTN: W. Rich

Kaman Tempo  
ATTN: W. McNamara  
ATTN: R. Rutherford  
ATTN: DASIAC

Kaman Tempo  
ATTN: DASIAC

Lutech, Inc  
ATTN: F. Tesche

Martin Marietta Corp  
2 cy ATTN: M. Griffith

Martin Marietta Corp  
ATTN: G. Freyer

McDonnell Douglas Corp  
ATTN: T. Ender

McDonnell Douglas Corp  
ATTN: S. Schneider

DEPARTMENT OF DEFENSE CONTRACTORS (Continued)

McDonnell Douglas Corp  
ATTN: M. Potter

Mission Research Corp  
ATTN: J. Lubell  
ATTN: EMP Group  
4 cy ATTN: C. Longmire  
4 cy ATTN: S. Chavin  
4 cy ATTN: W. Crevier  
4 cy ATTN: R. Kilb  
5 cy ATTN: Document Control

Mission Research Corp  
ATTN: A. Chodorow  
ATTN: L. McCormick

Mission Research Corp, San Diego  
ATTN: V. Van Lint

Mission Research Corporation  
ATTN: W. Stark  
ATTN: J. Lubell  
ATTN: W. Ware

Pacific-Sierra Research Corp  
ATTN: L. Schlessinger  
ATTN: H. Brode

R & D Associates  
ATTN: M. Grover  
ATTN: Document Control  
ATTN: C. Mo  
ATTN: P. Haas

R & D Associates  
ATTN: J. Bombardt  
ATTN: H. Mitchell

Rand Corp  
ATTN: LIB-D  
ATTN: W. Sollfrey

Rockwell International Corp  
ATTN: V. Michel  
ATTN: D/243-068, 031-CA31  
ATTN: J. Monroe  
ATTN: N. Rudie

Rockwell International Corp  
ATTN: B. White

Rockwell International Corp  
ATTN: B-1 DIV TIC (BA0B)

Rockwell International Corp  
ATTN: F. Shaw

Science Applications, Inc  
ATTN: R. Parkinson

Science Applications, Inc  
ATTN: N. Byrn

Science Applications, Inc  
ATTN: W. Chadsey

Sidney Frankel & Associates  
ATTN: S. Frankel

DEPARTMENT OF DEFENSE CONTRACTORS (Continued)

SRI International

ATTN: B. Gasten  
ATTN: E. Vance  
ATTN: A. Whitson

Sylvania Systems Group

ATTN: C. Thornhill  
ATTN: L. Blaisdell

Sylvania Systems Group

ATTN: C. Ramsbottom  
ATTN: J. Waldron  
ATTN: D. Flood  
ATTN: E. Motchok  
ATTN: A. Novenski  
ATTN: M. Nurefora

DEPARTMENT OF DEFENSE CONTRACTORS (Continued)

Systems, Science & Software, Inc

ATTN: A. Wilson

Teledyne Brown Engineering

ATTN: F. Leonard

Texas Tech University

ATTN: T. Simpson

TRW Defense & Space Sys Group

ATTN: W. Gargaro  
ATTN: L. Magnolia  
ATTN: O. Adams  
ATTN: H. Holloway  
ATTN: R. Plebuch